

Mechanisms of Mid- to Outer-Shelf Transport of Shoreline-Released Tracers

XIAODONG WU, FALK FEDDERSEN, AND SARAH N. GIDDINGS

Scripps Institution of Oceanography, University of California, San Diego, La Jolla, California

NIRNIMESH KUMAR

Department Civil and Environmental Engineering, University of Washington, Seattle, Washington

GANESH GOPALAKRISHNAN

Scripps Institution of Oceanography, University of California, San Diego, La Jolla, California

(Manuscript received 15 September 2019, in final form 1 May 2020)


ABSTRACT

Transport of shoreline-released tracer from the surfzone across the shelf can be affected by a variety of physical processes from wind-driven to submesoscale, with implications for shoreline contaminant dilution and larval dispersion. Here, a high-resolution wave–current coupled model that resolves the surfzone and receives realistic oceanic and atmospheric forcing is used to simulate dye representing shoreline-released untreated wastewater in the San Diego–Tijuana region. Surfzone and shelf alongshore dye transports are primarily driven by obliquely incident wave breaking and alongshore pressure gradients, respectively. At the midshelf to outer-shelf (MS–OS) boundary (25-m depth), defined as a mean streamline, along-boundary density gradients are persistent, dye is surface enhanced and time and alongshelf patchy. Using baroclinic and along-boundary perturbation dye transports, two cross-shore dye exchange velocities are estimated and related to physical processes. Barotropic and baroclinic tides cannot explain the modeled cross-shore transport. The baroclinic exchange velocity is consistent with the wind-driven Ekman transport. The perturbation exchange velocity is elevated for alongshore dye and cross-shore velocity length scales < 1 km (within the submesoscale) and stronger alongshore density gradient $\partial\rho/\partial y$ variability, indicating that along-front geostrophic flows induce offshore transport. This elevated $\partial\rho/\partial y$ is linked to convergent northward surface along-shelf currents (likely due to regional bathymetry), suggesting deformation frontogenesis. Both surfzone and shelf processes influence offshore transport of shoreline-released tracers with key parameters of surfzone and shelf alongcoast currents and alongshelf winds.

1. Introduction

Shoreline-released wastewater or runoff enters the surfzone (SZ, region of depth-limited wave breaking) delivering pathogens and contaminants to coastal regions, threatening the health and sustainability of coastal ecosystems (e.g., Ahn et al. 2005; Steele et al. 2018). For example, 35 million gallons per day (mgd) of untreated wastewater is released 10 km south of the Pacific U.S.–Mexico border at Pt. Bandera, Mexico (e.g., Orozco-Borbón et al. 2006). Shoreline tracer

dilution occurs through exchange across the surfzone, inner shelf, and farther offshore. Similarly, the coastal connectivity of intertidal invertebrates (e.g., Becker et al. 2007; Shanks et al. 2010) also requires cross-shelf exchange. A fraction of shoreline-released runoff or small river input is transported alongshore in the SZ, dependent on the flow rate and waves (Wong et al. 2013; Rodriguez et al. 2018). Obliquely incident wave breaking vertically mixes tracers (e.g., Feddersen 2012) and drives SZ alongshore currents (Longuet-Higgins 1970; Feddersen et al. 1998), transporting SZ tracer alongcoast up to 10 km (Grant et al. 2005; Feddersen et al. 2016). SZ tracers are cross-shore transported (exchanged) to the inner shelf due to transient rip currents (Hally-Rosendahl et al. 2014, 2015; Suanda and Feddersen 2015) or bathymetric inhomogeneities

 Denotes content that is immediately available upon publication as open access.

Corresponding author: Xiaodong Wu, x1wu@ucsd.edu

DOI: 10.1175/JPO-D-19-0225.1

© 2020 American Meteorological Society. For information regarding reuse of this content and general copyright information, consult the AMS Copyright Policy (www.ametsoc.org/PUBSReuseLicenses).

(e.g., [Castelle and Coco 2013](#); [Brown et al. 2015](#)). Inner-shelf tracer dilution occurs through transport to the midshelf (MS) and outer shelf (OS). Thus, understanding cross-shore transport pathways across these coastal regions is important for understanding the fate of shoreline-released tracer.

A variety of processes across a range of time scales can induce cross-shelf tracer transport, and relevant processes are reviewed here. On subtidal (>33 h) time scales, winds, waves, bathymetric variability, or regional-scale (10–100 km) alongshelf pressure gradients (APG) can drive offshore tracer transport. For an alongshelf uniform shelf, alongshelf wind driven Ekman layers induce cross-shore tracer transport for both stratified and unstratified conditions (e.g., [Austin and Lentz 2002](#); [Lentz and Fewings 2012](#)); however, as the depth becomes shallower than the Ekman depth, Ekman transport shuts down. Cross-shore winds also induce transport albeit weaker than alongshore winds (e.g., [Fewings et al. 2008](#); [Horwitz and Lentz 2016](#); [Wu et al. 2018](#)). Bathymetric variations such as headlands, capes, and shoals can steer mean flow at a variety of length scales (e.g., [Gan and Allen 2002](#); [Castelao and Barth 2006](#); [Radermacher et al. 2017](#)), inducing cross-shore transport. A barotropic APG-driven flow induces a bottom Ekman transport with a compensating interior cross-shore geostrophic current ([Lentz 2008](#); [Marchesiello and Estrade 2010](#)), yielding cross-shore exchange.

Semidiurnal and diurnal barotropic (BT, surface) and baroclinic (BC, internal) tides also play an important role in cross-shelf exchange (e.g., [Pineda 1994](#); [Walter et al. 2014](#)). Cross-shore dye transport is induced by nonzero covariance between the cross-shore velocity and dye over a tidal cycle, analogous to tidal pumping inducing estuary–ocean exchange (e.g., [Lerczak et al. 2006](#); [Geyer and MacCready 2014](#)). On the inner shelf, strong BT tides can induce residual flow via tidal rectification (e.g., [Ganju et al. 2011](#)). In the Southern California Bight (SCB), semidiurnal (e.g., [Lerczak et al. 2003](#); [Buijsman et al. 2012](#); [Kumar et al. 2016](#); [Sinnott et al. 2018](#)) and diurnal BC tides are ubiquitous ([Lerczak et al. 2001](#); [Nam and Send 2013](#); [Kumar et al. 2015](#)) even though the diurnal frequency is subcritical at SCB latitudes. The semidiurnal BC tide can drive an onshore cold-water transport through tidal pumping (e.g., [Walter and Phelan 2016](#)), and can cross-shore export heat from the nearshore ([Sinnott and Feddersen 2019](#)). BC tides enhance model simulated horizontal and vertical tracer dispersion in 30–50-m water depth ([Suanda et al. 2018](#)), and enhance mixing, reducing stratification ([Suanda et al. 2017](#)) and inducing residual cross-shelf flow. The diurnal internal tide is primarily responsible for the diurnal offshore

and onshore advection of a SCB beach-released dye ([Grimes et al. 2020](#)).

Submesoscale flows have $O(1)$ km length scales, are often seen as fronts and filaments, and have $O(1)$ or greater Rossby number $Ro = \zeta/f$ where ζ is the vertical relative vorticity and f is the local planetary vorticity (e.g., [McWilliams 2016](#)). Fronts and filaments can be a primary driver for offshore tracer transport hundreds of kilometers from shore (e.g., [Nagai et al. 2015](#)), and may be important in cross-shelf transport within 5 km of shore (e.g., [Romero et al. 2016](#)). Submesoscale flow variability is ubiquitous in coastal drifter observations (e.g., [Ohlmann et al. 2017](#)) and high-resolution coastal models (e.g., [Dauhajre et al. 2017](#)). Generation mechanisms of open ocean (deep water) submesoscale variability include mixed layer instability (e.g., [Boccaletti et al. 2007](#)), turbulent thermal wind balance (e.g., [McWilliams et al. 2015](#)), and deformation flow induced frontogenesis (e.g., [Hoskins 1982](#)). However, frontogenesis processes in shallow (relative to horizontal scales) and frictional coastal waters are less clear and understudied. In coastal environments, bathymetric variations (e.g., [Pringle 2002](#)) or wind forcing (e.g., [Tilburg and Garvine 2003](#)) can drive surface deformation flow that may induce frontogenesis.

As the effects of the Pt. Bandera shoreline-released untreated wastewater are unknown, we seek to understand the offshore transport pathways in the San Diego Bight using a realistic model that includes the surfzone. Regional studies include examination of San Diego Bay (SDB) tidal outflow (e.g., [Chadwick and Largier 1999](#)), Pt. Loma upwelling ([Roughan et al. 2005](#)), episodic small river plumes (e.g., [Warrick et al. 2007](#)), and the evolution of shoreline-released dye ([Hally-Rosendahl et al. 2014, 2015](#); [Grimes et al. 2020](#)). HF radar estimated regional currents reveal rich variability on length scales of ≈ 10 km with $O(1)$ Rossby number ([Kim 2010](#)). However, the HF radar cannot resolve length scales < 5 km. Dye observations within 1 km of shore in this region reveal spatial variability from 0.01 to 1 km ([Hally-Rosendahl et al. 2015](#); [Grimes et al. 2020](#)). Thus, within 10 km of shore, significant submesoscale flow variability is likely present.

Dye and drifters in realistic shelf models have been extensively used to study Lagrangian transport and dispersion processes (e.g., [Uchiyama et al. 2014](#); [Romero et al. 2013](#); [Giddings et al. 2014](#); [Romero et al. 2016](#); [Dauhajre and McWilliams 2019](#)), with varying grid resolutions. Shoreline larval dispersion patterns for the San Diego Bight were simulated with a realistic model at 600-m grid resolution ([Rasmussen et al. 2009](#)), but without a surfzone. A Lagrangian transport model forced with HF radar currents was used

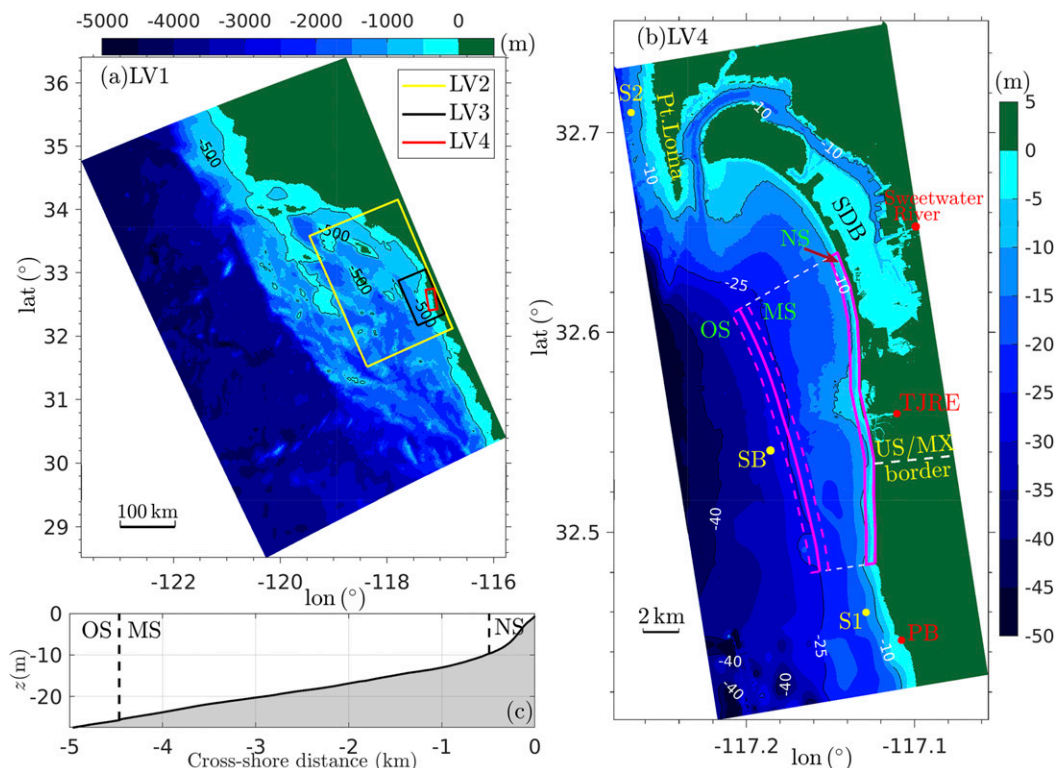


FIG. 1. (a) Bathymetry (color shading) of LV1 grid with outlines of the LV2 (yellow), LV3 (black), and LV4 (red) grids; (b) LV4 grid bathymetry and the delineation of the nearshore (NS), midshelf (MS) to outer-shelf (OS) boundary (solid magenta lines); (c) NS to OS bathymetry that is alongshore averaged following the NS domain. In (b), the dashed magenta lines denote the 1-km-wide MS–OS transition zone centered at the MS–OS boundary. The red dots denote freshwater sources Punta Bandera (PB), Tijuana River estuary (TJRE), and Sweetwater River within San Diego Bay (SDB). The yellow dots denote the South Bay Ocean outfall (SB) mooring site in 30-m depth and two selected sites (S1, S2) for current dynamics analysis. The U.S.–Mexico border and the headland Pt. Loma are also labeled.

to estimate Pt. Bandera exposure kernels (Kim et al. 2009). However, currents were unknown within 1–2 km of shore, surface trapped tracking, and objective mapping velocity smoothing lead to significant exposure uncertainty (Kim et al. 2010). Coupled wave and circulation models allow both the surfzone and shelf to be resolved (Kumar et al. 2012), which is crucial as shoreline-released tracer often is surfzone alongshore transported (Feddersen et al. 2016; Grimes et al. 2020).

Here, shoreline-released tracer is simulated from the SZ to the outer shelf in the San Diego Bight using a high-resolution wave–current coupled model with realistic forcing. The specific goal is to elucidate the principal mechanism(s) responsible for offshore tracer transport in the mid- to outer-shelf region using relatively simple metrics. The mechanisms considered include Ekman, barotropic and baroclinic tidal, and submesoscale flows. Analysis focuses on a 3-month (midsummer to fall) period characterized by weak to moderate winds, prevalent southerly incident surface gravity waves,

strong alongshore pressure gradients, and active internal waves. The model configuration and methods are given in section 2. The spatiotemporal tracer variability and transport are presented in section 3. Alongshore transport mechanisms are examined in section 4. Mechanisms for cross-shore transport across a MS–OS boundary are diagnosed in section 5. The relationships between key parameters governing dye transport and the role of other processes are discussed in section 6. Section 7 provides a summary.

2. Method

a. Model configuration

Surfzone and shelf circulation is simulated using the Coupled Ocean–Atmosphere–Wave–Sediment–Transport (COAWST) model system (Warner et al. 2010; Kumar et al. 2012). Three one-way nested parent models (from LV1 to LV2 to LV3) and one high-resolution child run (LV4, see Fig. 1a for the four grids) are run from

midsummer to early winter 2015 spanning a seasonal transition from summertime mostly southerly incident surface waves to wintertime mostly northerly incident waves. The LV1–LV3 runs employ the Regional Ocean Modeling System (ROMS; [Shchepetkin and McWilliams 2005](#)), a three-dimensional, hydrostatic model using a stretched terrain-following vertical coordinate ([Shchepetkin and McWilliams 2005](#)). The LV4 run includes surface gravity waves by coupling ROMS with the Simulating Waves Nearshore model (SWAN; [Booij et al. 1999](#)), a phase-averaged wave model that solves the wave action balance equation. NAM surface flux fields (wind stress, heat, and precipitation) are used for all grids. Over the 5-month simulation period, the 21 days of NAM data gaps are filled with the Coupled Ocean–Atmosphere Mesoscale System (COAMPS) fields. The vertical viscosity and diffusivity are estimated using a k – ϵ scheme ([Umlauf and Burchard 2003](#)). A logarithmic bottom drag scheme is used with a bottom roughness $z_0 = 0.1$ cm, following [Kumar et al. \(2015\)](#). The horizontal eddy viscosity and diffusivity are constant at $0.5 \text{ m}^2 \text{ s}^{-1}$. For the LV4 model, SWAN and ROMS are two-way coupled at 10-min intervals allowing current effects on waves and wave effects on currents through surfzone wave breaking and vortex force.

1) PARENT RUN GRIDS AND SETUP

The model grids of the three parent runs downscale from 2-km horizontal resolution for the SCB (LV1 with 253×390 horizontal grid cells), to 600-m resolution resolving the southern SCB (LV2 with 266×398 grid cells), and to 200-m resolution for the greater San Diego shelf region (LV3 with 251×413 grid cells) (see [Fig. 1a](#)). All three domains have 40 terrain-following vertical levels with enhanced resolution near the surface and bottom. Grid bathymetry is derived from the 3-arc-second NOAA/NGDC coastal relief dataset.

The outermost LV1 domain inherits the boundary and initial conditions from the California State Estimate (CASE) solution, an implementation of the z -level, primitive equation MIT general circulation model (MITgcm; [Marshall et al. 1997](#)). CASE assimilates a variety of remote and in situ observations, including satellite altimetry data, satellite measured sea surface temperature, temperature and salinity profiles from Argo and Spray glider, expendable bathythermograph (XBT) temperature transects, autonomous pinniped bathythermograph (APB) temperature profiles, and shipboard CTD profiles ([Zaba et al. 2018](#)). Daily averaged CASE solutions are linearly interpolated from z - to σ -level coordinates, and then horizontally interpolated onto the LV1 model grid and open boundaries. CASE does not include tides.

Barotropic tidal elevation and velocities of 10 tidal constituents (M_2 , S_2 , N_2 , K_2 , O_1 , P_1 , Q_1 , K_1 , M_4 , and M_6) are prescribed on the LV1 open boundaries with the amplitudes and phases from the ADCIRC tidal database ([Westerink et al. 1993](#)), allowing generation and propagation of internal waves within the model domain (e.g., [Kumar et al. 2015](#); [Suanda et al. 2017](#); [Kumar et al. 2019](#)).

The LV1 solutions provide initial and boundary conditions for LV2. Subsequently, the LV2 solutions are used for LV3, and the LV3 solutions are used for LV4. Chapman and Flather radiation boundary conditions are used for the sea level and the barotropic (depth independent) velocity ([Flather 1976](#); [Chapman 1985](#)). For the baroclinic (depth dependent) flow and tracers, the Orlanski radiation condition is used together with nudging to constrain the interior solution to the parent ([Marchesiello et al. 2001](#)). In LV1–LV3 domains, the nudging time scale for outgoing baroclinic flow and tracers along open boundaries is 365 day^{-1} , and the nudging time scale for the incoming baroclinic flow and tracers is 6 h^{-1} . All solutions are saved at 1-h intervals. The LV1 model was initialized at 1200 UTC 1 July 2015, and the LV2 and LV3 models were initialized at 1200 UTC 4 July and 1200 UTC 7 July, respectively, allowing 3–4 days of spinup in each parent grid.

2) LV4 RUN GRID AND SETUP

The LV4 grid (with 486×1142 grid cells, area $15 \times 36 \text{ km}^2$) spans the outer shelf to surfzone in the southern San Diego Bight ([Fig. 1b](#)), which includes the SDB and the headland Pt. Loma to the north. Southward of the SDB entrance, the shoreline first curves and then straightens, passing the Tijuana River Estuary (TJRE), the U.S.–Mexico border and Punta Bandera (PB) within Mexico. South of the curvature, the bathymetry is largely alongshore uniform, except for a broad shoal seaward of TJRE that extends offshore ([Fig. 1b](#)). The LV4 grid cross-shore resolution increases from 110 m at the western open boundary to 8 m along the coastline, and alongshore resolution varies from 110 m at the southern and northern open boundaries to 8 m near the TJRE mouth. The stretched vertical domain has 15 levels and the NOAA 1/3-arc-second coastal digital elevation is used for bathymetry.

The LV4 SWAN model has 25 frequencies between 0.04 and 0.29 Hz and 42 directional bands spanning from 145° to 355° (wave direction in nautical convention), covering all potential incidence angles. The shoreline normal direction south of 32.6°N is approximately 265° . CDIP wave model frequency-directional wave spectra are used for open boundary conditions ([O'Reilly et al. 2016](#)). The wave-breaking parameter $\gamma = 0.5$ is used

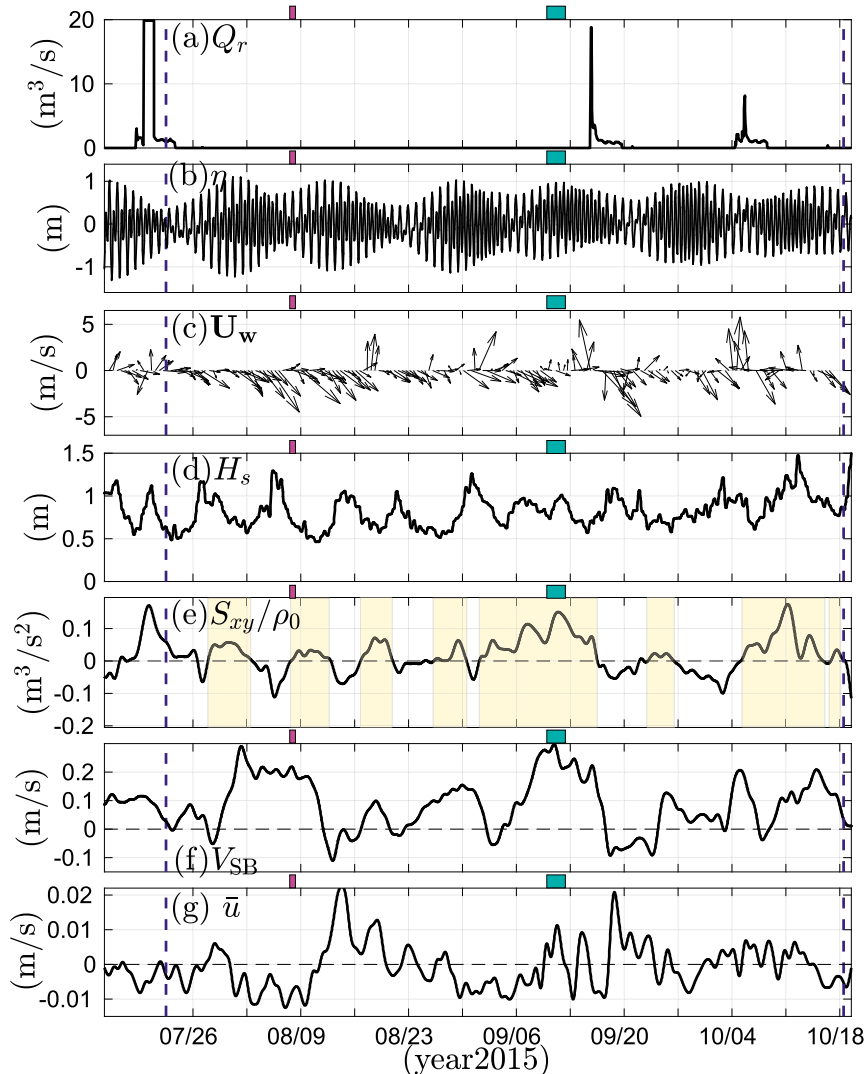


FIG. 2. Time series of (a) freshwater discharge rate Q_r at TJRE, (b) sea surface elevation η at SB, (c) wind velocity vectors U_w at SB, (d) significant wave height H_s at SB, (e) subtidally averaged off-diagonal radiation stress tensor S_{xy}/ρ_0 (positive corresponds to southerly incident waves) at SB, (f) subtidal depth-averaged alongshore current at SB V_{SB} , and (g) subtidal depth- and along-MS-OS-boundary averaged cross-boundary velocity $\bar{u}(t)$ [Eq. (5a)]. In (e), the yellow shading indicates times of southerly incident waves. In all panels, the two vertical blue dashed lines delineate the analysis period. The small magenta rectangle corresponds to the time period shown in Fig. 3 and the cyan rectangle indicates the time period shown in Fig. 14.

following Kumar et al. (2015). Wind-wave generation is also included. Note that because SWAN is a wave-averaged model, the LV4 simulation has bathymetric rip currents but does not have transient rip currents which require a wave-resolving model (Feddersen 2014).

The LV4 ROMS component receives freshwater inputs from PB, TJRE, and the Sweetwater River within SDB (see Fig. 1b). The parent grids do not receive freshwater input. At PB, freshwater, representing untreated wastewater, is released onto the beach at a

constant discharge rate $Q_r = 1.53 \text{ m}^3 \text{ s}^{-1}$ (35 mgd). TJRE freshwater discharge is given by in situ measurements at International Boundary and Water Commission (IBWC) gauging station and discharge primarily occurs during rainfall events (Fig. 2a). Additional coastal runoff emanating from the Sweetwater River within SDB is also incorporated in LV4. The Sweetwater River discharge rate is approximately estimated by multiplying the observed flow rate at a nearby river (San Diego River) by the ratio of the drainage area (Archfield and Vogel 2010).

As PB and Sweetwater River inflow temperatures are unknown, a 30-day low-pass-filtered in situ Tijuana River (Oneonta Slough) temperature measurement is applied for all three sources to remove weekly and higher-frequency variations that could be variable among sites. Passive tracer (dye) of constant concentration $D = 1$, representing untreated wastewater, is added to the PB freshwater discharge. The off-diagonal radiation stress tensor term S_{xy} (Longuet-Higgins 1970; Feddersen et al. 1998) is estimated as

$$S_{xy} = -\frac{1}{16}\rho_0 g H_s^2 \frac{c_g}{c} \sin(\theta_w) \cos(\theta_w), \quad (1)$$

where θ_w denotes the mean wave angle relative to the shoreline normal, H_s denotes the significant wave height, $\rho_0 = 1025 \text{ kg m}^{-3}$ denotes a reference density, and c_g and c denote the group and phase speeds, respectively. A positive S_{xy} corresponds to southerly incident waves, which drives northward alongshore surfzone currents. Subtidal filtering is performed with the PL64 filter (Limeburner et al. 1985) with 33-h cutoff.

The LV4 coupled model was initialized on 12 July 2015, allowing 5 days of parent LV3 model spinup, and integrated to 25 December 2015. Relevant time series are shown in Fig. 2. Modeled barotropic tidal amplitudes (Fig. 2b) and phases of M_2 , S_2 and K_1 compare well with in situ measurements (not shown here). NAM winds (Fig. 2c) are consistent with nearby buoy winds (not shown) and are frequently southward directed with low ($|\mathbf{U}_w| < 5 \text{ m s}^{-1}$) to moderate $5\text{--}8 \text{ m s}^{-1}$ speeds. Wave and alongshelf velocities are given at a 30-m-depth central location denoted SB (Fig. 1b). At SB, H_s varies between 0.5 and 1.5 m (Fig. 2d). The LV4 simulation has multiple periods of southerly incident waves (i.e., $S_{xy} > 0$, yellow shading in Fig. 2e). These wave statistics compare well with local buoy observations, consistent with previous Southern California results (O'Reilly et al. 2016). At SB, the subtidal depth-averaged alongshore flow V_{SB} ranges from -0.1 to 0.3 m s^{-1} and is mostly northward (positive) (Fig. 2f). The modeled dye concentration and dye transport are analyzed during the analysis period from 22 July to 18 October 2015 (dashed line in Fig. 2). This allows a 10-day period of LV4 dye spinup (22 days from LV1 initialization) at which point LV4 domain averaged enstrophy has equilibrated. After 18 October, occurrences of northerly incident incoming waves end northward transport of PB dye.

b. Analysis methods

To facilitate the cross- and alongshore dye transport analysis, two regions are defined (Fig. 1b). The first region is the nearshore (NS) spanning from the shoreline with a cross-shore width of $L_x^{(NS)} = 500 \text{ m}$. The NS

reaches 10-m water depth and includes both the SZ and the shallow portion of the inner shelf. The NS southern boundary is located 4.5 km north of PB allowing dye to adjust upon release and the alongshore length is $L_y^{(NS)} = 18 \text{ km}$. The northern extent is set to avoid the rapidly curving isobath farther north. The second region is the MS–OS boundary (Fig. 1b) with mean depth of 25 m (Fig. 1c) and alongshore length of $L_y^{(MS,OS)} = 15.3 \text{ km}$. The MS–OS boundary curves offshore such that southern and northern ends are approximately 3.1 and 6.3 km from the shoreline, respectively (white dashed lines in Fig. 1b). As offshore transport can be bathymetrically induced, the MS–OS boundary was chosen such that the depth-averaged and time-averaged (over the analysis period) flow across all parts of the MS–OS boundary is zero (MS–OS boundary is a mean streamline). Note, at any time step, the depth and along-boundary averaged cross-boundary flow is not necessarily zero. Analysis of cross-shore dye transport will be performed on the MS–OS boundary. To facilitate alongshore analysis, a MS–OS transition zone is defined centered at the MS–OS boundary with a width of $L_x^{(MS/OS)} = 1 \text{ km}$ (dashed magenta, Fig. 1b).

Hereafter, the cross-shore (x , positive onshore) and alongshore (y , positive northward) directions are locally defined as the normal to and parallel to the MS–OS boundary. Time averages (over the analysis period) are denoted with $\langle \cdot \rangle$. Standard deviations are represented by $\text{std}(\cdot)$. Because dye is positive definite and does not have a Gaussian distribution, the time-averaged dye $\langle D \rangle$ is based on a logarithmic average such that $\langle D \rangle = 10^{(\log_{10} D)}$ (e.g., Hally-Rosendahl et al. 2014). Temporal mean plus (minus) standard deviation of dye are defined as $(\langle D \rangle_+, \langle D \rangle_-) = (10^{(\log_{10} D) + \text{std}(\log_{10} D)}, 10^{(\log_{10} D) - \text{std}(\log_{10} D)})$. Within NS the dye is volume averaged ($\overline{D}^{(NS)}$).

Averaging operators are defined for analysis along the MS–OS boundary. For a variable ψ , an along-MS–OS boundary and depth-average $\overline{\psi}^{yz}$ is defined as

$$\overline{\psi}^{yz} = \frac{1}{L_y^{(MS,OS)} \overline{d}^{(MS,OS)}} \int_{-h}^{\eta} \int_0^{L_y^{(MS,OS)}} \psi \, dy \, dz, \quad (2)$$

where the along-boundary (y) integral is over the MS–OS boundary length and the average MS–OS boundary total depth $\overline{d}^{(MS,OS)} = \overline{h}^{(MS,OS)} + \eta$ (the average still water depth is $\overline{h}^{(MS,OS)} = 25.0 \text{ m}$). The along-boundary integral is only calculated over the wet portion of the MS–OS boundary, thus $\overline{\psi}^{yz}$ is an area average through the MS–OS y – z surface. In addition, an along-boundary average $\overline{\psi}^y$ is defined as

$$\overline{\psi}^y = \frac{1}{L_x(z)} \int_0^{L_x^{(MS,OS)}} \psi \, dx, \quad (3)$$

where, because the MS–OS boundary has variable depth, $L(z)$ is the along-boundary length of the wet portion of the MS–OS boundary at each z level. If the z level is always wet, then $L = L_y^{(MS,OS)}$.

The cross-MS–OS-boundary velocity u is decomposed into three components,

$$u(y, z, t) = \bar{u}(t) + \tilde{u}(z, t) + u'(y, z, t), \quad (4)$$

representing the depth- and along-boundary averaged transport \bar{u} , the along-boundary averaged baroclinic (vertically varying) velocity \tilde{u} , and the along-boundary perturbation velocity u' . These are defined as

$$\bar{u}(t) = \overline{\mathbf{u}_L^{(MS,OS)} \cdot \mathbf{n}}^{yz}, \quad (5a)$$

$$\tilde{u}(z, t) = \overline{(\mathbf{u}_L^{(MS,OS)} \cdot \mathbf{n})}^y - \bar{u}, \quad (5b)$$

$$u'(y, z, t) = \mathbf{u}_L^{(MS,OS)} \cdot \mathbf{n} - \bar{u}(t) - \tilde{u}(z, t), \quad (5c)$$

where \mathbf{u}_L is the model Lagrangian horizontal velocity (Eulerian plus Stokes drift derived from the wave model) and \mathbf{n} is the normal to the MS–OS boundary. The time average of the first component $\langle \bar{u} \rangle = 0$ by definition as the MS–OS boundary is a streamline of the depth- and time-averaged velocity. Overall, \bar{u} fluctuates between -0.01 and 0.02 m s^{-1} (Fig. 2g), attributed to bathymetric induced transport due to the significant inverse correlation ($r = -0.4$) between \bar{u} and V_{SB} , consistent with mass conservation. The along-boundary averaged baroclinic velocity \tilde{u} [Eq. (5b)] has by definition $\overline{\tilde{u}}^{yz} = 0$. The third component u' [Eq. (5c)] is associated with short-scale (relative to $L_y^{(MS,OS)}$) variability and by definition $\overline{u'}^{yz} = 0$. This MS–OS boundary decomposition is also applied to the dye and density,

$$D(y, z, t) = \bar{D}(t) + \tilde{D}(z, t) + D'(y, z, t), \quad (6a)$$

$$\rho(y, z, t) = \bar{\rho}(t) + \tilde{\rho}(z, t) + \rho'(y, z, t). \quad (6b)$$

At the MS–OS boundary, the total cross-shore dye transport Q_x is

$$\begin{aligned} Q_x(t) &= \int_{-h}^{\eta} \int_0^{L_y^{(MS,OS)}} (\mathbf{u}_L^{(MS,OS)} \cdot \mathbf{n}) D \, dy \, dz \\ &= L_y^{(MS,OS)} \bar{D}(t) \overline{(\mathbf{u}_L^{(MS,OS)} \cdot \mathbf{n})}^{yz}, \end{aligned} \quad (7)$$

where again the along-boundary integral is only calculated over the wet portion. The Q_x is composed of three components $Q_x = \bar{Q}_x + \tilde{Q}_x + Q'_x$ defined as

$$\bar{Q}_x(t) = \bar{u}(t) \bar{D}(t) L_y^{(MS,OS)} \bar{d}^{(MS,OS)}, \quad (8a)$$

$$\tilde{Q}_x(t) = \overline{\tilde{u}(z, t) \tilde{D}(z, t)}^{yz} L_y^{(MS,OS)} \bar{d}^{(MS,OS)}, \quad (8b)$$

$$Q'_x(t) = \overline{u'(y, z, t) D'(y, z, t)}^{yz} L_y^{(MS,OS)} \bar{d}^{(MS,OS)}. \quad (8c)$$

Note that the terms $\overline{u' \bar{D}}^{yz}$, $\overline{u' \tilde{D}}^{yz}$, $\overline{\bar{u} D'}^{yz}$, $\overline{\bar{u} \tilde{D}}^{yz}$, and $\overline{\bar{u} D'}^{yz}$ are all zero by definition, which is also confirmed numerically. For the baroclinic and along-boundary fluctuating dye transports, corresponding MS–OS boundary exchange velocities are defined as

$$\tilde{U}_{ex}(t) = \frac{\tilde{Q}_x(t)}{\bar{D}(t) L_y^{(MS,OS)} \bar{d}^{(MS,OS)}}, \quad (9a)$$

$$U'_{ex}(t) = \frac{Q'_x(t)}{\bar{D}(t) L_y^{(MS,OS)} \bar{d}^{(MS,OS)}}. \quad (9b)$$

The \tilde{U}_{ex} is ascribed to baroclinic flow developed over a regional ($<10 \text{ km}$) scale, while U'_{ex} is attributed to shorter-scale processes with significant u' and D' . Both \tilde{U}_{ex} and U'_{ex} are only estimated when dye is present at the MS–OS boundary ($\bar{D} > 10^{-6}$), which removes 7% of the data. Note, the \bar{Q}_x exchange velocity is similarly defined but just equals $\bar{u}(t)$.

Within NS and the MS–OS transition zone, an along-region averaged along-region dye transport velocity is similarly defined as

$$V_*^{(r)}(t) = \frac{1}{L_y^{(r)}} \int_0^{L_y^{(r)}} \left(\frac{\int_{x_1}^{x_2} \int_{-h}^{\eta} v_L D \, dz \, dx}{\int_{x_1}^{x_2} \int_{-h}^{\eta} D \, dz \, dx} \right) dy, \quad (10)$$

where (r) represents NS or MS/OS, x_1 and x_2 represent the offshore and onshore region locations [e.g., for NS, $(x_1, x_2) = (-L_x^{(NS)}, 0)$, and for MS–OS, x_1 and x_2 represent the dashed lines bounding 500 m on either side of the MS–OS boundary in Fig. 1b], and the Lagrangian alongshore velocity is v_L . We note that dye mass balances within control volumes close, confirming the dye and dye transport estimates. To average over the tidal and higher-frequency variability, the quantities \bar{D} , Q_x , V_* , \tilde{U}_{ex} , and U'_{ex} are subtidally filtered.

3. Results: Spatiotemporal dye variability

a. Example of an offshore dye transport event

Upon Pt. Bandera shoreline release at concentration $D = 1$, dye is advected at a range of spatiotemporal scales spanning surfzone and shelf. Four snapshots of dye D , density anomaly $\sigma_t = \rho - 1000 \text{ kg m}^{-3}$, and currents covering 18 h are presented to show the spatiotemporal evolution of an offshore dye transport event (Fig. 3). Event winds and wind stresses were weak

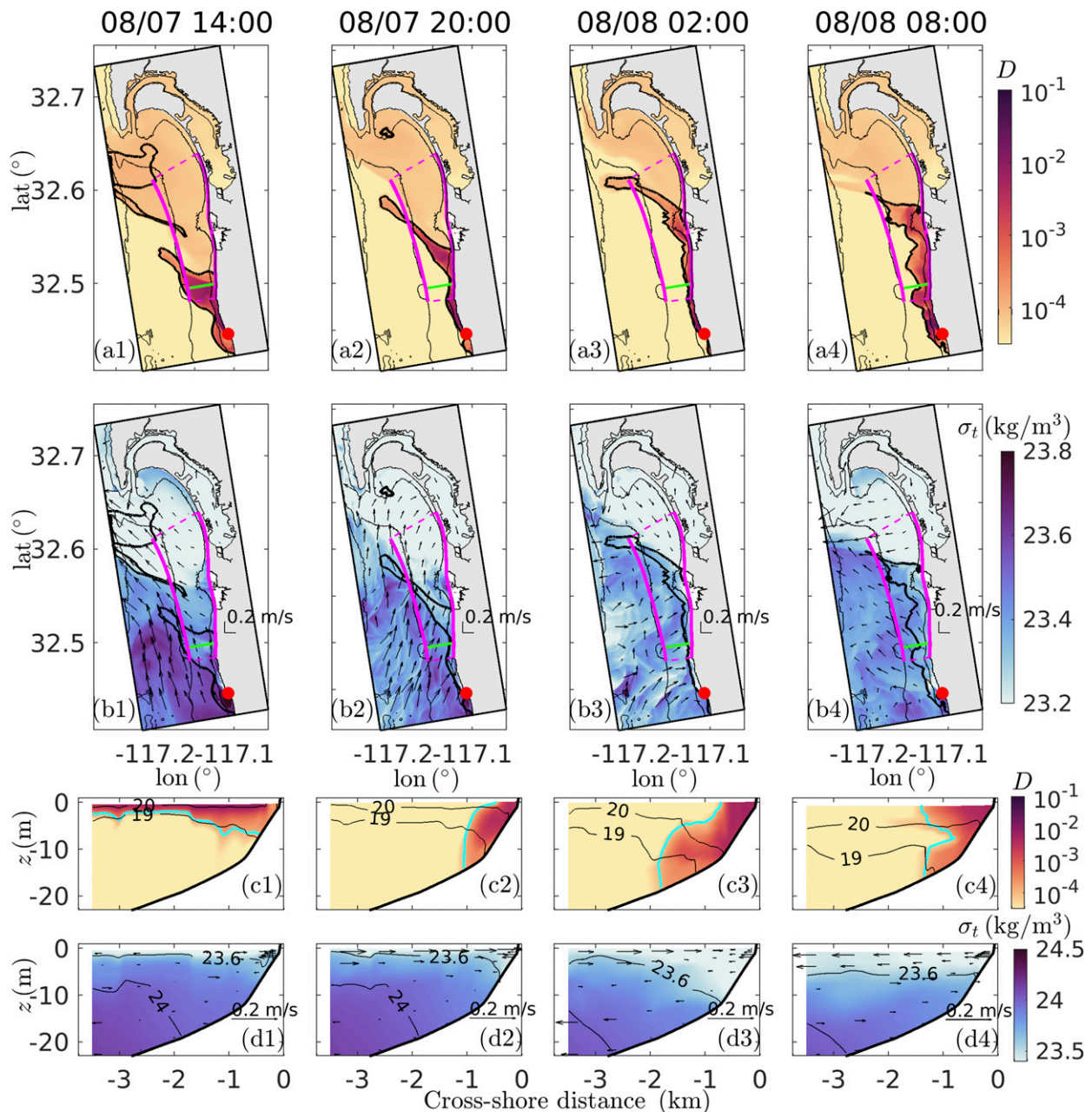


FIG. 3. Snapshots of an 18-h offshore dye transport event at (left to right) four times at 6-h intervals. Surface distribution of (a) dye concentration D (color shading) and (b) density anomaly σ_t (color shading) and surface current velocity (vectors). Cross-shore and vertical profile of (c) D (color shading) and isotherms (line contour) and (d) density anomaly σ_t (color shading and black contour) and cross-shore current velocity (vectors) along a chosen transect. The magenta curve outlines the NS and MS-OS boundary regions. The green line in (a) and (b) shows the transect location. The thick black contour in (a) and (b) and the cyan contour in (c) correspond to $D = 10^{-4}$.

(Fig. 2c) with average wind onshore at 2 m s^{-1} and a $\pm 1 \text{ m s}^{-1}$ diurnal rotating sea breeze. At the event start, southerly incident waves (yellow shading in Fig. 2e) have just arrived driving northward NS dye transport (Figs. 3a1–4). Dye concentration is low ($D < 10^{-4}$) on the northern shelf and within SDB (Figs. 3a1–4). An

alongshore density gradient is present and the shelf surface currents are primarily northward (Figs. 3b1–4).

At the first time step (1400 UTC 7 August, Fig. 3a1), surface D is advected northward. A high concentration ($D > 10^{-4}$) and meandering dye patch extends seaward and obliquely crosses the MS-OS boundary with width

(where $D > 10^{-4}$) of 3.8 km and peak $D = 2.7 \times 10^{-3}$. At the dye offshore leading edge, the offshore current is 0.1 m s^{-1} . The surface density perturbation has additional small-scale variability (Fig. 3b1). Along the cross-shore transect (green line in Fig. 3a1), dye is concentrated within upper 5-m layer above the thermocline $T = 19^\circ\text{C}$ (Fig. 3c1). The cross-shore current is relatively weak (magnitude $< 0.05 \text{ m s}^{-1}$, Fig. 3d1). Six hours later (2000 UTC 7 August, Fig. 3a2), the surface dye patch has been advected farther northward and elongated into a filament with MS–OS boundary width of 580 m at high peak concentration $D = 2.4 \times 10^{-4}$. At the dye offshore leading edge, the offshore current is 0.07 m s^{-1} . The elongation is due to a positive $\partial u/\partial x$ associated with a negative $\partial v/\partial y$ (not shown), which also enhances the alongshore density gradient at the MS–OS boundary (Fig. 3b2). At the cross-shore transect, the surface layer onshore current strengthens (reaching 0.2 m s^{-1} , Fig. 3d2), leading to near-surface onshore dye transport. As a result, south of the filament, surface D is completely contained within the NS (Fig. 3a2). Subsurface, the $T = 19^\circ\text{C}$ isotherm and dye layer deepen to $z = -14 \text{ m}$ within 1 km from shore mostly within the NS (see the vertical dye contour $D = 10^{-4}$ in Fig. 3c2).

Twelve hours later (0200 UTC 8 August, Fig. 3a3), the dye filament has been advected farther north, orienting more cross-shore. Seaward of the MS–OS boundary, the filament is advected offshore by the surface currents at 0.2 m s^{-1} (Fig. 3b3). At the MS–OS boundary, the dye filament has a width of 1.3 km with max $D = 1.4 \times 10^{-4}$. South of the filament, surface dye is almost completely contained within the NS (Fig. 3a3). At the cross-shore transect, the onshore (offshore) current within the surface (bottom) layer is well developed (reaching 0.1 m s^{-1} at surface, Fig. 3d3). Both the 20°C isotherm (Fig. 3c3) and 23.6 kg m^{-3} isopycnal (Fig. 3d3) are tilted down toward shore, and the near-bed dye is advected offshore to $z = -18 \text{ m}$, but remains within 1.75 km of shore. Eighteen hours later (0800 UTC 8 August), the dye filament decays (Figs. 3a4,b4). Onshore of the MS–OS boundary and south of the strong alongshore density gradient, surface dye is advected offshore extending the $D = 10^{-4}$ contour onto the MS–OS boundary, as surface and bottom cross-shore currents reverse (Figs. 3c4,d4). Subsurface, the isotherms and isopycnals flatten and the near bottom dye is advected back onshore. As wind forcing was weak, weak Ekman transport is expected. The short alongshore scales of this offshore dye transport event suggest that submesoscale flows are responsible for the offshore dye transport.

b. Dye and density statistics

The spatial variability of temperature T , salinity S , density anomaly σ_t , and dye statistics is investigated next

(Fig. 4). For depth $< 25 \text{ m}$, the time-mean temperature $\langle T \rangle$ is elevated on the northern shelf and SDB by $\approx 0.5^\circ\text{C}$ relative to the southern shelf near PB (Fig. 4a1). This alongshore $\langle T \rangle$ signal is in the parent LV3 results (not shown here), indicating it is not due to the temperature of the LV4 freshwater discharge. The largest temperature standard deviation $\text{std}(T)$ ($> 1.4^\circ\text{C}$) occurs in the nearshore ($h < 10 \text{ m}$, Fig. 4b1), due to stronger diurnal warming and cooling in shallow water, without a clear alongshore gradient. Relatively low $\langle S \rangle$ and high $\text{std}(S)$ (> 0.3) occur near the three freshwater sources (Figs. 4a2,b2). The shelf $\langle S \rangle$ also has a north–south gradient, fresher to the north (Fig. 4a2), resulting in an alongshelf gradient of $\langle \sigma_t \rangle$ (Fig. 4a3) with northern $\langle \sigma_t \rangle$ lower by 0.2 kg m^{-3} . The $\text{std}(\sigma_t)$ ($> 0.3 \text{ kg m}^{-3}$) is elevated near freshwater sources and in the nearshore ($h < 10 \text{ m}$), implying combined contributions from S and T . Along the MS–OS boundary, the $\langle \sigma_t \rangle$ gradient is $5.8 \times 10^{-6} \text{ kg m}^{-4}$ but the $\text{std}(\sigma_t)$ is largely alongshore uniform. The surface dye statistics $\langle D \rangle_-$ and $\langle D \rangle_+$ (defined in section 2b, Figs. 4a4,b4) highlight the upper and lower ranges of typical dye, varying from 10^{-2} to 10^{-5} . Both show northward dye transport and dilution away from PB, resembling a diffusive plume, with higher concentrations onshore, implying net offshore dye transport (Fig. 4b4). Onshore of the MS–OS boundary, $\langle D \rangle_+$ is about 100 times that of $\langle D \rangle_-$.

Large values of the surface density horizontal gradient magnitude $|\nabla_{HP}\rho|$ and $\text{rms}(\zeta/f) > 1$ indicate fronts and filaments and high Rossby numbers. Elevated values of both quantities are seen in the NS (Figs. 4a5,b5), attributed to surface wave breaking, bathymetric irregularities, freshwater inputs and surface heat fluxes. Within the NS $\text{rms}(\zeta/f) > 3$ suggesting an active submesoscale (Fig. 4b5). Both statistics are also elevated near the SDB mouth. Onshore of the MS–OS boundary, the TJRE shoal has elevated $\text{rms}(|\nabla_{HP}\rho|)$ and $\text{rms}(\zeta/f)$, while for the rest of the domain, the distribution of both is largely alongshore uniform. At the MS–OS boundary, $\text{rms}(|\nabla_{HP}\rho|) = 1.3(\pm 0.2) \times 10^{-4} \text{ kg m}^{-4}$ and $\text{rms}(\zeta/f) = 0.8(\pm 0.1)$, consistent with other high-resolution coastal simulations (e.g., Dauhajre et al. 2017; Dauhajre and McWilliams 2019), and indicates that submesoscale dynamics may be important in this region. Although the PB ($1.5 \text{ m}^3 \text{ s}^{-1}$) and TJRE (Fig. 2a) freshwater input rates are typically small, salinity gradients contribute an average $\approx 30\%$ to the $\text{rms}(|\nabla_{HP}\rho|)$, and are elevated during time of TJRE freshwater input (Fig. 2a).

The temporal and alongshore variability of MS–OS boundary surface density perturbation ρ' [Eq. (6b)] and dye D are examined in Fig. 5. The ρ' has a persistent negative south to north gradient (Fig. 5a), consistent with Fig. 4a3. Significant variability is present with times

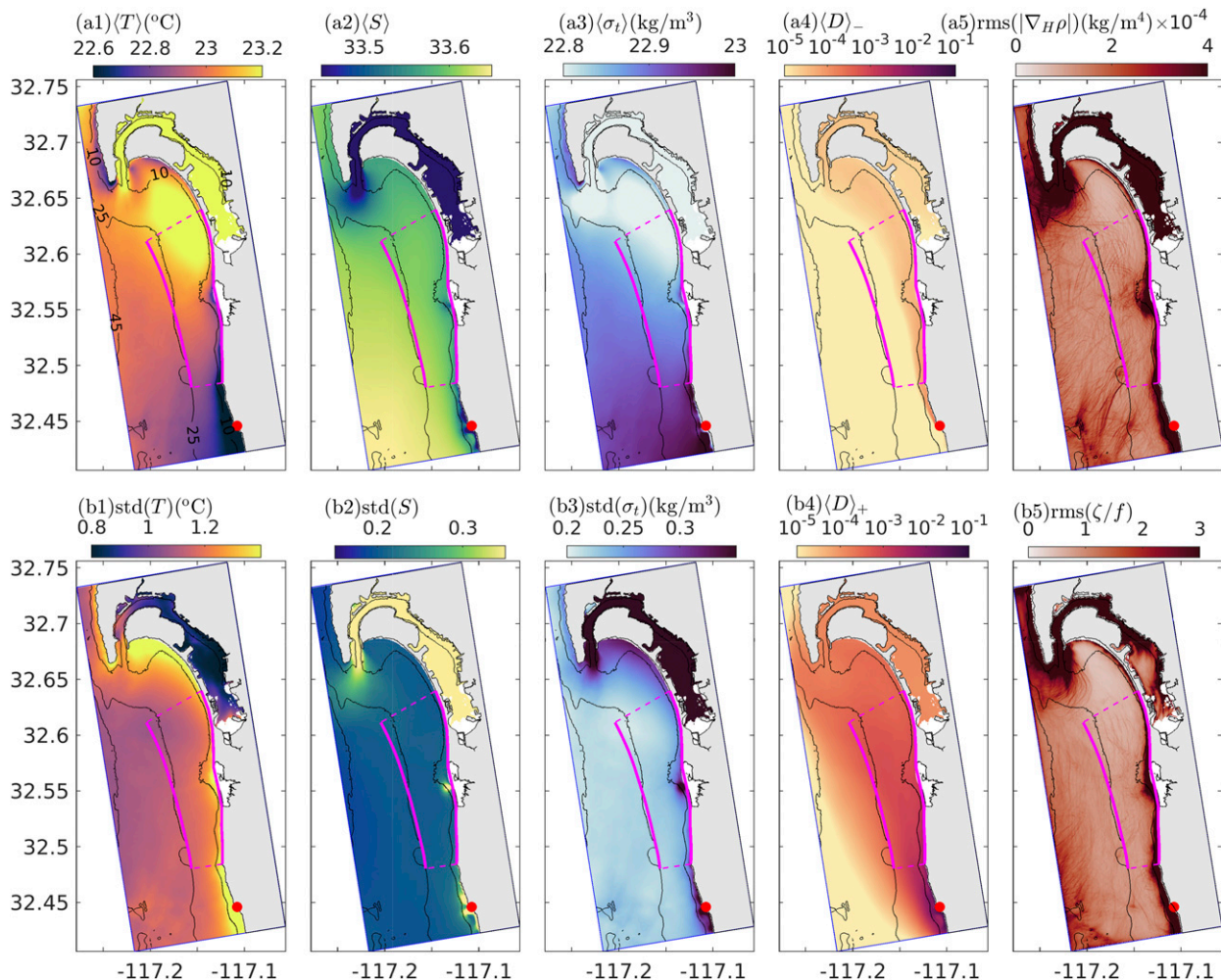


FIG. 4. Horizontal distribution of (top) temporal mean and (bottom) standard deviation of (a1),(b1) surface T ($^{\circ}\text{C}$); (a2),(b2) S ; (a3),(b3) density anomaly σ_t (kg m^{-3}); (a4),(b4) typical high and low surface dye concentrations $\langle D \rangle_-$ and $\langle D \rangle_+$; (a5) rms of horizontal surface density gradient $\nabla_{HP}\rho$ (kg m^{-4}); and (b5) normalized rms surface relative vorticity $\text{rms}(\zeta)/f$. Black contours denote the isobaths $h = [10, 25, 45]$ m. The magenta line outlines the NS to MS-OS boundary. The red dot denotes the PB source.

of alongshore uniform (e.g., 6–10 October, Fig. 5a) or step function like ρ' (9 August, near 32.56°N). MS-OS boundary surface dye also has very strong variability (Fig. 5b). The northern end almost always has $D > 10^{-5}$, consistent with the mean dye fields (Figs. 4a4,b4). The temporal D variability is largely diurnal to subtidal. The along-boundary D variability is often patchy with a few km or less length scales, consistent with this offshore dye ejection event (Fig. 3). Dye can be present along much of the boundary (26 July), only in a limited region (9 August), or nearly absent ($D < 10^{-5}$, 10 September).

The logarithmic scale in Fig. 5b obscures the strong along-boundary dye gradients, and the dye patchiness suggests that the MS-OS boundary dye has relatively short alongshore length scales. A MS-OS boundary alongshore surface dye length scale $L_D^{(\text{MS,OS})}$ is defined as

$$L_D^{(\text{MS,OS})}(t) = \left\{ \frac{[D(y,t) - \overline{D}^y(t)]^{2^y}}{\left[\frac{\partial D(y,t)}{\partial y} \right]^{2^y}} \right\}^{1/2}, \quad (11)$$

which is evaluated at each time step when MS-OS boundary averaged dye is $> 10^{-6}$, and also subtidally filtered (Fig. 5c). The $L_D^{(\text{MS,OS})}$ varies from 0.3 to 4 km, confirming that the MS-OS boundary D is patchy, and is also consistent with the example event 0.58–3.8-km D length scales (Fig. 3). The subtidal $L_D^{(\text{MS,OS})}$ varies from 0.4 to 3 km. Length scales for density ρ and cross-boundary velocity u are similarly estimated along the MS-OS boundary (L_u and L_ρ) which also vary between 0.4 and 4 km, jointly suggesting the importance of submesoscale dynamics (e.g., McWilliams 2016).

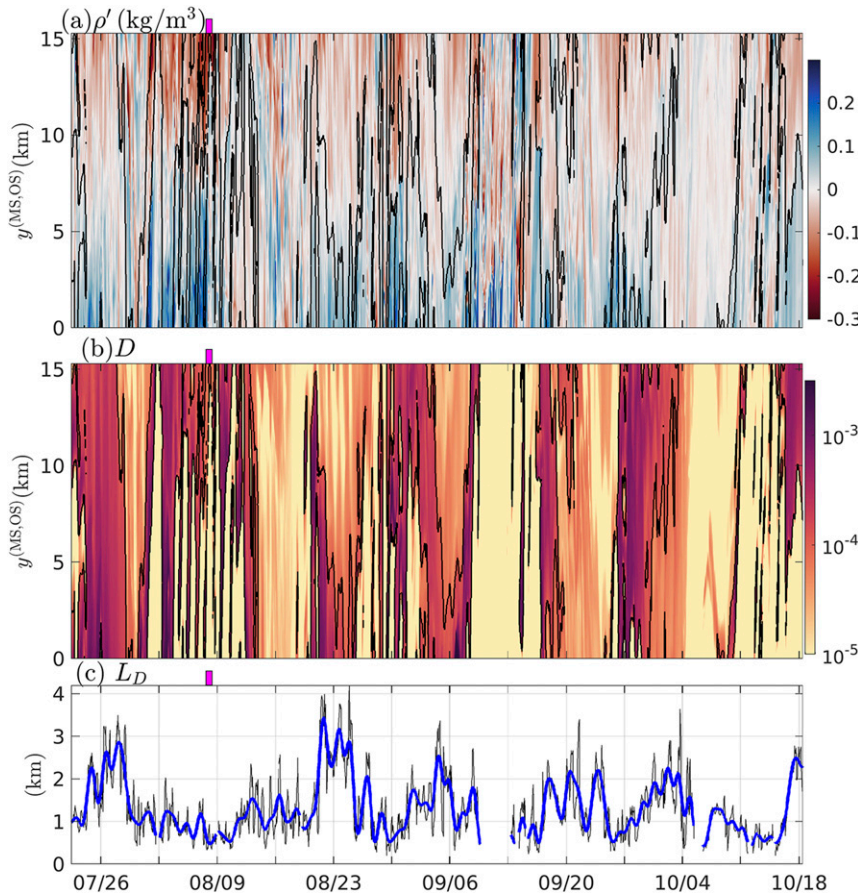


FIG. 5. Hovmöller diagram (time and alongshore distance) of surface (a) density perturbation ρ' [Eq. (6b)] and (b) dye along the MS–OS boundary. In (a) and (b), the black contour denotes $D = 10^{-4}$. (c) Time series of alongshore dye length scale L_D along MS–OS boundary both hourly (black) and subtidally filtered (blue). Gaps are when MS–OS boundary-averaged $D < 10^{-6}$. The small magenta rectangle indicates the time period shown in Fig. 3.

The vertical structure of the time mean and std of $\tilde{\rho}$, \tilde{D} , and \tilde{u} , and the square root of time alongshore mean of squared ρ' , D' , and u' are examined at the MS–OS boundary (Fig. 6). During the summer and early fall, the MS–OS boundary is strongly stratified (Fig. 6a1) with time mean $\partial\langle\tilde{\rho}\rangle/\partial z \approx 0.03 \text{ kg m}^{-4}$ (or $N \approx 0.02 \text{ s}^{-1}$) that is two orders of magnitude or larger than the along-boundary stratification $\text{rms}(|\nabla_{H\rho}|)$ (Fig. 4a5). Associated with the vertical stratification, time mean baroclinic dye $\langle\tilde{D}\rangle$ is surface intensified and decays exponentially downward with 6.3-m decay scale (Fig. 6a2). The temporal std of $\tilde{\rho}$ and \tilde{D} is elevated at the surface and reaches a minima at 10-m water depth (Figs. 6a1,a2). The time-mean cross-boundary baroclinic velocity $\langle\tilde{u}\rangle$ has magnitude usually $< 0.01 \text{ ms}^{-1}$ and a three-layer profile with offshore directed flow at surface and bottom, and onshore flow in between (Fig. 6a3). The temporal std of the subtidally averaged \tilde{u} varies between 0.01 and

0.03 ms^{-1} , is elevated at surface (Fig. 6a3), and has a variability minimum near $z = -10 \text{ m}$. The \tilde{u} profile statistics are consistent with a combined Ekman and mode-1 baroclinic process. Note, the subtidal filter removes baroclinic tidal velocities, which will be discussed in section 5a.

In addition, significant temporal and alongshore variability is evident in ρ' , D' , and u' (Figs. 6b1–b3) through their time and alongshore standard deviation (i.e., $\langle\rho'^2\rangle^{1/2}$). The $\langle\rho'^2\rangle^{1/2}$ is elevated in the upper 10 m near 0.07 kg m^{-3} (Fig. 6b1), about 10% of the top to bottom $\langle\tilde{\rho}\rangle$ difference (Fig. 6a1), but is comparable to the $\tilde{\rho}$ temporal std, suggesting significant alongshore density fluctuations, consistent with Fig. 5a. Similarly, $\langle D'^2\rangle^{1/2}$ is near-surface elevated, decaying with a $\approx 10 \text{ m}$ vertical scale. The $\langle D'^2\rangle^{1/2}$ is comparable to the \tilde{D} std, consistent with Fig. 5b, and the $O(1) \text{ km}$ inferred $L_D^{(\text{MS,OS})}$ (Fig. 5c). The $\langle u'^2\rangle^{1/2}$ increases from 0.02 ms^{-1} near bed

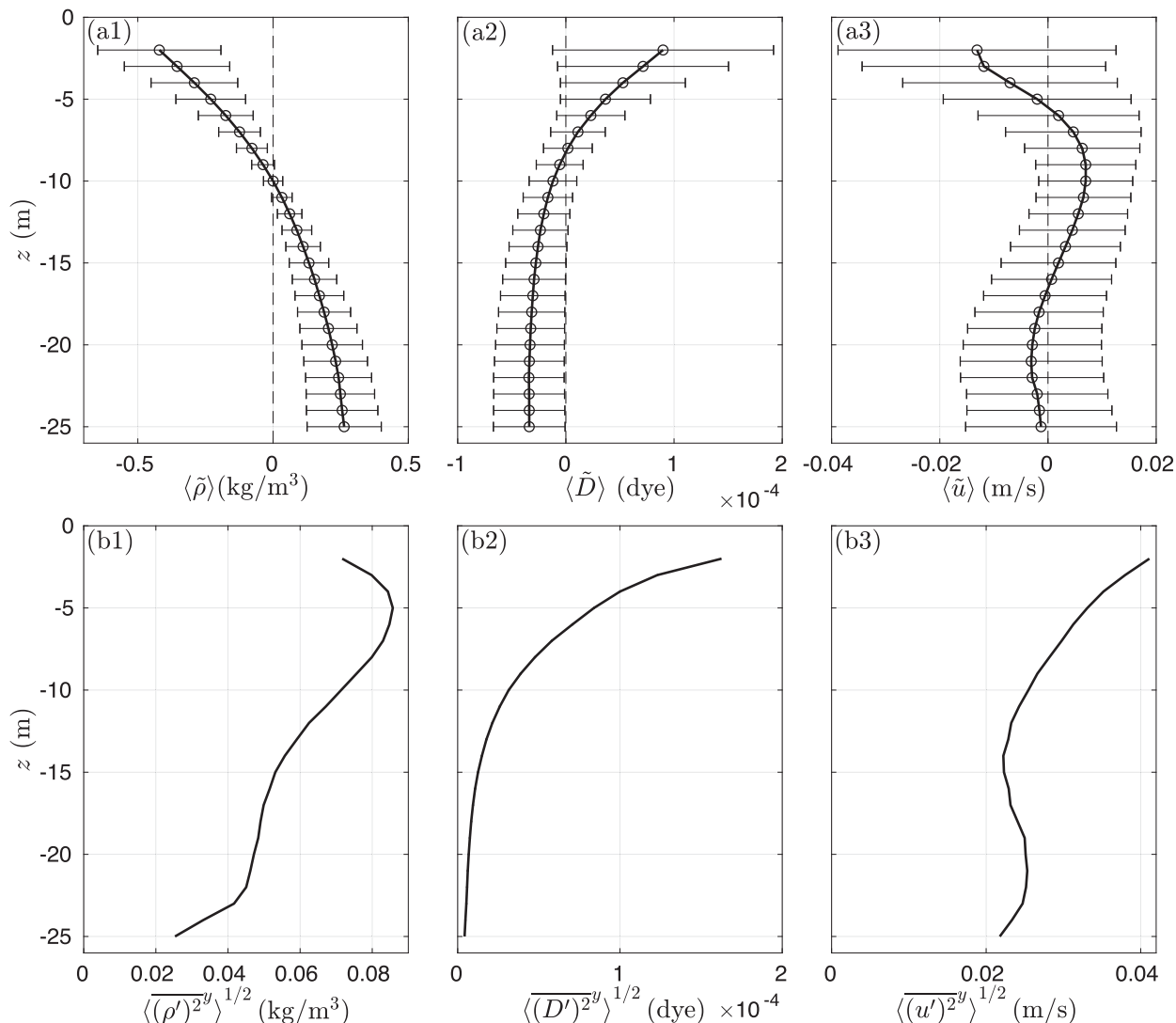


FIG. 6. MS–OS boundary statistics as a function of the vertical z : (top) time mean (circles) and standard deviation (horizontal bars) of subtidally filtered baroclinic (a1) $\bar{\rho}$, (a2) \bar{D} , and (a3) \bar{u} ; (bottom) root-time-alongshore mean of squared along-boundary perturbation quantities (b1) $\langle \bar{\rho}'^{2y} \rangle^{1/2}$, (b2) $\langle \bar{D}'^{2y} \rangle^{1/2}$, and (b3) $\langle \bar{u}'^{2y} \rangle^{1/2}$.

to 0.04 m s^{-1} near surface (Fig. 6b3), slightly larger than the temporal std of \bar{u} (Fig. 6a3). This decomposition makes clear that MS–OS boundary offshore dye transport can occur due to both alongshore-uniform baroclinic processes and alongshore variable processes.

c. Dye and dye transport temporal evolution

During the analysis period, seven individual south swell events (i.e., $S_{xy} > 0$, Fig. 2e) occur (yellow shading in Figs. 7 and 2e) each with distinct subtidal NS-averaged dye $\bar{D}^{(\text{NS})}$ peaks mostly $>10^{-3}$ (Fig. 7a). In between south swell events, $\bar{D}^{(\text{NS})}$ drops by a factor of 10–100. The MS–OS boundary mean \bar{D} [Eq. (6a)] is significantly weaker ($\approx 10\%$) than $\bar{D}^{(\text{NS})}$ (Fig. 7a). The \bar{D} peaks are

qualitatively lagged relative to $\bar{D}^{(\text{NS})}$ peaks, indicating a transport pathway. The depth std of \bar{D} (\bar{D}^z)^{1/2} largely follows and is usually slightly above \bar{D} (Fig. 7a), as dye is surface intensified. During peaks in offshore \bar{D} , the alongshore-depth std of D' (\bar{D}'^{yz})^{1/2} usually is just larger than both \bar{D} and (\bar{D}^z)^{1/2} indicating along-boundary dye patchiness. The 10–12 September time period (cyan rectangle in Fig. 7a) is notable because $\bar{D}^{(\text{NS})}$ is strongly elevated ($>10^{-3}$) for an extended duration yet the MS–OS boundary \bar{D} , (\bar{D}^z)^{1/2}, and (\bar{D}'^{yz})^{1/2} are all weak (mostly $<10^{-6}$), and will be discussed in more detail in section 6c.

The depth- and along-boundary mean cross-MS–OS-boundary dye transport \bar{Q}_x [Eq. (8a)] switches sign

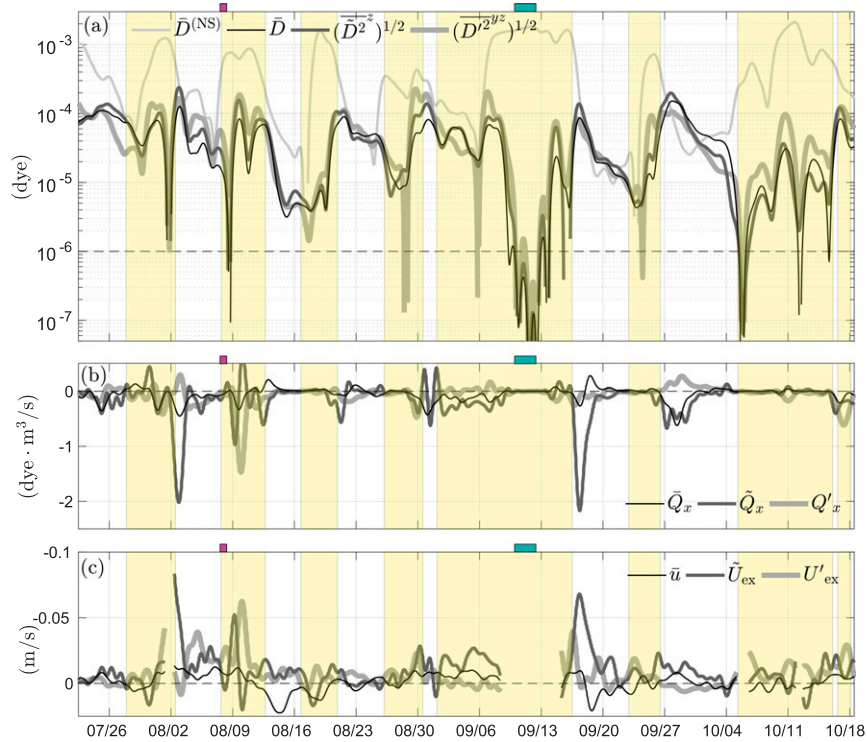


FIG. 7. Time series of (a) NS volume-averaged dye $\bar{D}^{(NS)}$, depth- and along-MS-OS-boundary averaged dye \bar{D} [Eq. (6a)], depth std of \bar{D} [$(\bar{D}^2)^{1/2}$], and along-boundary and depth std of D' [$(D'^2)^{1/2}$]; (b) MS-OS-boundary dye transport components \bar{Q}_x , \tilde{Q}_x , and Q'_x [Eq. (8)], and (c) MS-OS-boundary averaged cross-shore velocity \bar{u} , and baroclinic and along-boundary perturbation exchange velocities \tilde{U}_{ex} and U'_{ex} [Eq. (9)]. The small magenta rectangle indicates the time period shown in Fig. 3 and the cyan rectangle indicates the time period shown in Fig. 14.

frequently (Fig. 7b), has a time mean of $-0.05 \text{ dye m}^3 \text{ s}^{-1}$ (representing 19% of total transport) and std of $0.12 \text{ dye m}^3 \text{ s}^{-1}$, and is attributed to bathymetrically driven flows. The baroclinic dye transport \tilde{Q}_x [Eq. (8b)]

is the largest of the three dye transports and is primarily offshore (i.e., negative, Fig. 7d) with time mean of $-0.15 \text{ dye m}^3 \text{ s}^{-1}$ (57% of total transport) and std of $0.33 \text{ dye m}^3 \text{ s}^{-1}$ over a number of quasi intermittent

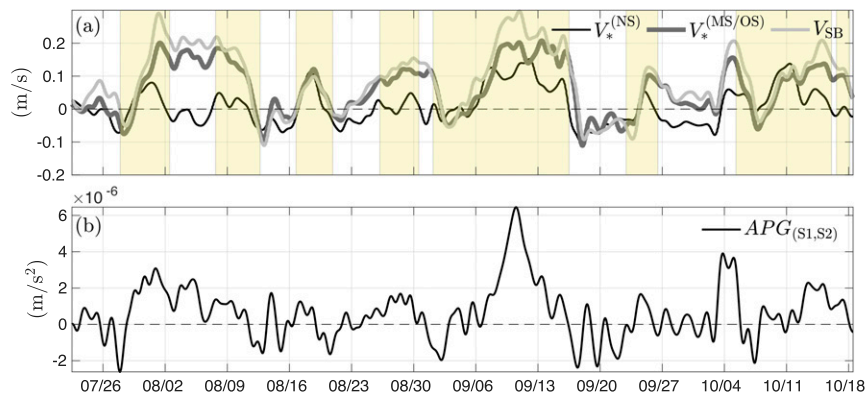


FIG. 8. Time series of subtidal (a) alongshore dye transport velocity within NS $V_*^{(NS)}$ and the MS-OS transition zone $V_*^{(MS/OS)}$, as well as the depth-averaged alongshore current velocity at SB V_{SB} . (b) Time series of subtidal barotropic alongshore pressure gradient (normalized by density) between sites S1 and S2 (see Fig. 1b for locations). The yellow shading in (a) represents periods of positive S_{xy} .

events. The along-boundary perturbation transport Q'_x [Eq. (8c)] is also intermittent and fluctuates with a std of $0.17 \text{ dye m}^3 \text{ s}^{-1}$ relatively large relative to the time mean of $-0.06 \text{ dye m}^3 \text{ s}^{-1}$ (24% of total transport). Overall Q'_x is the second-largest term although occasionally it is bigger than \tilde{Q}_x (e.g., 10 August, Fig. 7b). Nearly all of the net (time averaged) offshore Q'_x occurs prior to 1 September, and for this period time mean $\langle Q'_x \rangle = 0.11 \text{ dye m}^3 \text{ s}^{-1}$ and $\langle \tilde{Q}_x \rangle = 0.13 \text{ dye m}^3 \text{ s}^{-1}$ are similar. For the post 1 September time period, $\langle Q'_x \rangle$ is negligible but $\langle \tilde{Q}_x \rangle$ is the same. The baroclinic (\tilde{U}_{ex}) and alongshore perturbation (U'_{ex}) cross-shore dye exchange velocities [Eqs. (9)] are largely negative (seaward directed, Fig. 7c), varying between 0.02 and -0.07 m s^{-1} . The time mean $\langle \tilde{U}_{\text{ex}} \rangle$ and $\langle U'_{\text{ex}} \rangle$ both are -0.01 m s^{-1} with $\text{std}(\tilde{U}_{\text{ex}}) = 0.013 \text{ m s}^{-1}$ slightly larger than $\text{std}(U'_{\text{ex}}) = 0.010 \text{ m s}^{-1}$. Thus, for the time period when \tilde{U}_{ex} and U'_{ex} could be calculated (when $\bar{D} > 10^{-6}$), both baroclinic processes and alongshore-perturbation processes have similar transport potential. Next, we explore the mechanisms driving alongshore and cross-MS–OS-boundary dye transports.

4. Alongshore dye transport mechanisms

The 500-m-wide NS region (Fig. 1b) typically has a 100-m-wide surfzone for the incident wave heights (Fig. 2d). Surfzone alongshore currents are driven by the breaking of obliquely incident waves (e.g., Longuet-Higgins 1970; Feddersen et al. 1998). The nearshore subtidal alongshore dye transport velocity $V_*^{(\text{NS})}$ [Eq. (10)] varies between -0.1 and 0.1 m s^{-1} (Fig. 8) corresponding to 9–17 km day^{-1} . Consistent with surfzone-dominated transport, the subtidal $V_*^{(\text{NS})}$ is largely positive (northward directed) during southerly wave events (yellow shading in Fig. 8a) and is highly correlated with S_{xy}/ρ_0 with squared correlation of $r^2 = 0.63$ ($p < 0.05$), best fit slope of ≈ 1 , and near-zero intercept. This best fit slope is factor of 2 consistent with a simple surfzone alongshore wave forcing and linear bottom friction balance assuming a 100-m surfzone width and linear drag coefficient of $3 \times 10^{-3} \text{ m s}^{-1}$ (e.g., Lentz et al. 1999). In contrast, $V_*^{(\text{NS})}$ was only weakly related ($r^2 = 0.14$, $p > 0.05$) to the alongshore wind stress. This demonstrates the primary role of obliquely incident surface gravity waves in driving alongshore NS dye transport over long (tens of kilometers) distances consistent with previous observations and modeling (Grant et al. 2005; Hally-Rosendahl et al. 2015; Hally-Rosendahl and Feddersen 2016; Feddersen et al. 2016). Other mechanisms such as wind driven currents in the outer NS, tidal currents, and shear dispersion can play a secondary role.

The 1-km-wide MS–OS transition zone has a subtidal alongshore dye transport velocity $V_*^{(\text{MS/OS})}$ [Eq. (10)]

that is significantly stronger than within the nearshore $V_*^{(\text{NS})}$ (Fig. 8a). The subtidal $V_*^{(\text{MS/OS})}$ is strongly correlated to the subtidal depth-averaged SB alongshelf velocity V_{SB} (Fig. 2f) with $r^2 = 0.92$ ($p < 0.05$) and at 75% the magnitude of V_{SB} (Fig. 8a), attributed to a reduced current (i.e., current shear) onshore of SB. Note, alongshore transport is larger than cross-shore transport as $V_*^{(\text{MS/OS})}$ is larger than the three U_{ex} . The analysis period is characterized by weak to moderate alongshore wind forcing (Fig. 2c). Subtidal alongshore wind stress is uncorrelated ($r^2 = 0.05$, $p > 0.05$) with V_{SB} and has magnitude 4 times too weak (using a linear friction of $3 \times 10^{-4} \text{ m s}^{-1}$; Lentz and Winant 1986) to explain V_{SB} , suggesting that other dynamics are driving the alongshelf current. Previous SCB studies (e.g., Hickey et al. 2003) have shown that during fall the barotropic APG is a significant driver of alongshelf flow even in 15 m depth (Lentz and Winant 1986). The subtidal barotropic APG is estimated from north to south in 15-m depth within the LV4 domain (S1 and S2 in Fig. 1b). The resulting barotropic APG largely varies between $\pm 2 \times 10^{-6} \text{ m s}^{-2}$, is mostly northward directed as the alongshelf flow and largely varies on fortnightly time scales (Fig. 8b). The barotropic APG is reasonably correlated with V_{SB} ($r^2 = 0.49$, $p < 0.05$) and has the correct magnitude for a frictionally balanced flow (using 15-m depth and linear friction of $3 \times 10^{-4} \text{ m s}^{-1}$). Thus, the regional alongshore current which drives midshelf alongshore dye transport is primarily driven by the barotropic APG.

5. Cross-shore dye transport mechanisms at the MS–OS boundary

As baroclinic \tilde{Q}_x [Eq. (8b)] and the along-boundary perturbation Q'_{ex} [Eq. (8c)] were the largest transport terms, here, we separately examine potential mechanisms for \tilde{Q}_x and Q'_x , including BT and BC tides, wind-driven Ekman transport, barotropic alongshore pressure gradients, and submesoscale flows. Recall that \tilde{Q}_x can be due to alongshore uniform but baroclinic flows such as Ekman transport or BC tides, while Q'_x can be induced by alongshore variable flows over the 15-km-long MS–OS boundary. To elucidate the hydrodynamic processes, we compare the dye exchange velocity components \tilde{U}_{ex} [Eq. (9a)] and U'_{ex} [Eq. (9b)] with relatively simple derived hydrodynamic velocities for each process.

a. Barotropic and baroclinic tidal cross-shore transport

One potential mechanism for the cross-shore dye transport across the MS–OS boundary could be barotropic (BT) and baroclinic (BC) tides. In the example

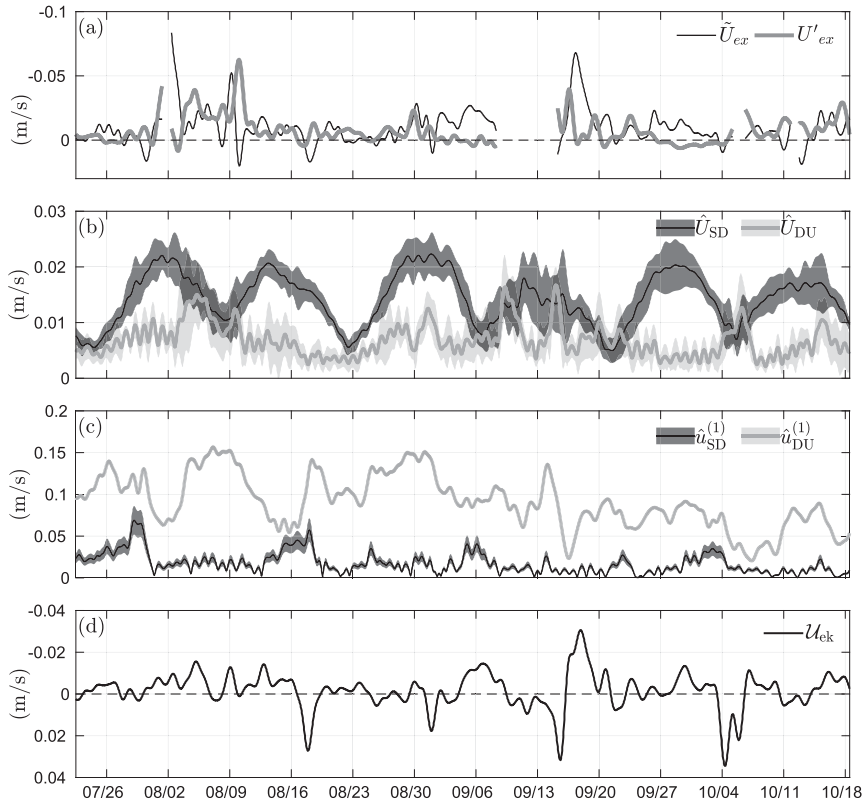


FIG. 9. Time series of MS-OS boundary (a) baroclinic \tilde{U}_{ex} and along-boundary perturbation U'_{ex} cross-shore dye exchange velocities. (b) Barotropic cross-shore velocity amplitude [Eq. (A1)] in the semidiurnal $\tilde{U}_{SD}^{(1)}$ and diurnal $\tilde{U}_{DU}^{(1)}$ band, and (c) surface baroclinic cross-shore velocity amplitude in the semidiurnal $\hat{u}_{SD}^{(1)}$ and diurnal $\hat{u}_{DU}^{(1)}$ band. (d) Estimated Ekman velocity U_{ek} vertically averaged over the upper 8 m to the Ekman depth. In (b) and (c), the shading represents the alongshore std.

offshore dye transport event (Fig. 3), the diurnal BC tide advects surface dye onshore and offshore and vertically, similar to the observed evolution of shoreline-released dye near 32.59°N during the analysis period (Grimes et al. 2020). If BT and BC tidal exchange mechanisms (see section 1) were a primary driver of the cross-shore exchange, then the subtidal BC exchange velocity \tilde{U}_{ex} would be less than and correlated with the slowing varying tidal velocity amplitude. Here, in both the semidiurnal (SD) and diurnal (DU) bands, alongshore mean (and std) MS-OS tidal surface velocity amplitudes are estimated for BT (\hat{U}_{SD} , \hat{U}_{DU}), and BC ($\hat{u}_{SD}^{(1)}$, $\hat{u}_{DU}^{(1)}$) tides (see the appendix). Both BC and BT tidal variability are largely along-boundary coherent (Figs. A1b,c), thus the tidal velocity amplitudes are compared to the MS-OS boundary baroclinic \tilde{U}_{ex} exchange velocity. However, as some BT and BC tide alongshore phase variation is present, tidal velocity amplitudes are also compared to the alongshore perturbation U'_{ex} exchange velocity.

The relationship of barotropic tidal velocity amplitudes and \tilde{U}_{ex} and U'_{ex} are examined first (Figs. 9a,b).

The alongshore averaged \hat{U}_{SD} fluctuates fortnightly between 0.01 and 0.02 m s⁻¹ with very small std along the boundary, indicating that the single BT velocity amplitude is representative. However, \hat{U}_{SD} is much weaker than and uncorrelated ($r^2 = 0.005$, $p > 0.05$, see Table 1) with \tilde{U}_{ex} (Figs. 9a,b). The alongshore mean \hat{U}_{DU} is generally < 0.01 m s⁻¹ and poorly correlated ($r^2 = 0.02$, $p < 0.05$) with \tilde{U}_{ex} . Similarly, U'_{ex} is uncorrelated with \hat{U}_{SD} , and not significantly correlated with \hat{U}_{DU} ($r^2 = 0.18$, $p > 0.05$), albeit \hat{U}_{DU} is half the magnitude of U'_{ex} . Thus, BT tides cannot be the main driver of the \hat{Q}_x or Q'_x cross-MS-OS-boundary dye transports. For BC tides,

TABLE 1. Squared correlation r^2 between the dye exchange velocity components and BT and BC semidiurnal and diurnal tidal velocity amplitudes as well as upper 8-m averaged Ekman velocity U_{ek} . The values above 95% confidence level are highlighted in bold.

	\hat{U}_{SD}	\hat{U}_{DU}	$\hat{u}_{SD}^{(1)}$	$\hat{u}_{DU}^{(1)}$	U_{ek}
\tilde{U}_{ex}	0.005	0.02	0.03	0.007	0.40
U'_{ex}	0.000	0.18	0.04	0.01	0.012

the surface DU BC tidal amplitude $\hat{u}_{\text{DU}}^{(1)}$ is generally larger than the surface SD amplitude $\hat{u}_{\text{SD}}^{(1)}$ (Fig. 9c), similar to previous observations (e.g., Kim et al. 2011; Johnston and Rudnick 2015) and modeling (e.g., Kumar et al. 2015) in the SCB. The $\hat{u}_{\text{SD}}^{(1)}$ is smaller than and uncorrelated ($r^2 = 0.03$, $p > 0.05$) with \tilde{U}_{ex} (Figs. 9a,c). The alongshore averaged $\hat{u}_{\text{DU}}^{(1)}$ is comparable in magnitude (reaches 0.15 m s^{-1}) to \tilde{U}_{ex} (Figs. 9a,c), but is uncorrelated ($r^2 = 0.007$, $p > 0.05$). Similarly, the alongshore perturbation U'_{ex} is uncorrelated with $\hat{u}_{\text{SD}}^{(1)}$ and $\hat{u}_{\text{DU}}^{(1)}$ (see Table 1). Thus, BC tides also cannot be the main driver of the \tilde{Q}_x or Q'_x cross-MS–OS-boundary dye transports.

b. Wind-driven Ekman cross-shore transport

Wind-driven Ekman transport is a potential mechanism for offshore dye transport. Here, wind-driven Ekman surface velocity at the MS–OS boundary is estimated following Ekman (1905) and compared with the dye exchange velocity \tilde{U}_{ex} . Conceptually, Ekman transport is considered an alongshore uniform and baroclinic process. Thus, if the offshore dye transport \tilde{Q}_x were due to Ekman transport, surface Ekman velocities should be of similar magnitude and correlated to \tilde{U}_{ex} .

For a steady, alongshore-uniform shelf with no along-shelf pressure gradients, shelf currents have an Ekman component (balancing friction) and alongshelf geostrophic component (balancing the cross-shelf pressure gradient) such that the depth-averaged cross-shore velocity is zero (Ekman 1905). For constant depth h , steady conditions, a no slip seafloor boundary condition, no stratification, and a constant eddy viscosity A_v , Ekman's analytic solution is used to estimate the (cross- and along-mean MS–OS boundary) velocity [$U_{\text{ek}}(z)$, $V_{\text{ek}}(z)$] (following Estrade et al. 2008):

$$U_{\text{ek}}(z) + iV_{\text{ek}}(z) = (1 - i) \frac{\tau_x + i\tau_y}{\rho_0 \sqrt{2fA_v}} \frac{\sinh[m(z+h)]}{\cosh(mh)} - \frac{iV_g \cosh(mz)}{\cosh(mh)}, \quad (12)$$

where $i = \sqrt{-1}$, (τ_x, τ_y) are the (subtidal) wind stress components (estimated from SB), $m = (1 + i)(f/2A_v)^{1/2}$, and V_g is the alongshelf geostrophic component obtained from the condition that the depth integrated cross-shore transport is zero. A constant $A_v = 2.5 \times 10^{-3} \text{ m}^2 \text{ s}^{-1}$ is used based on the depth- and time-averaged modeled eddy viscosity at SB, a value consistent with Suanda et al. (2017). Neglected transient effects in the Ekman velocity (12) are weak as subtidal winds vary on synoptic time scales. The Ekman depth $(2A_v/f)^{1/2} = 8 \text{ m}$ is consistent with the $z \approx 10 \text{ m}$ location of minimum \tilde{u} and \tilde{D} variability (Figs. 6a2,a3). A vertically averaged (over the upper 8 m) Ekman velocity is defined as $U_{\text{ek}}(t)$ for

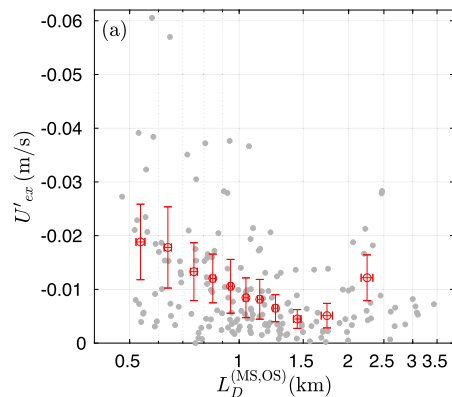


FIG. 10. Scatterplot (gray) with binned means (red) of MS–OS boundary exchange velocity component U'_{ex} vs along-boundary dye length scale $L_D^{(\text{MS,OS})}$. Both values are subtidally filtered, gray points are shown only every 8 h for visual clarity, and the binned means have 120-h points each. The subtidal (and binned mean) squared correlation is $r^2 = 0.06$ ($r^2 = 0.32$, $p < 0.05$).

comparison to \tilde{U}_{ex} . With the predominant southward wind (Fig. 2c), surface U_{ek} is primarily negative (Fig. 9d). The correlation is maximum at zero time lag between U_{ek} and \tilde{U}_{ex} . A least squares fit between U_{ek} and \tilde{U}_{ex} yields a near-one slope of 0.97 with significant $r^2 = 0.40$ ($p < 0.05$), indicating that Ekman transport is a principal driver for the baroclinic cross-MS–OS-boundary transport \tilde{Q}_x .

The time mean $\langle \tilde{u} \rangle(z)$ has a three-layer profile (Fig. 6a3); however, $U_{\text{ek}}(z)$ [Eq. (12)] has a two-layer profile. This difference together with the moderate r^2 between U_{ek} and \tilde{U}_{ex} may result from the assumptions built into [Eq. (12)] or from other processes (e.g., advection). We note that the barotropic APG is mostly northward directed (Fig. 8b) which would induce near-bed offshore Ekman transport and onshore return flow in the remaining water column (e.g., Lentz 2008). Thus, APG driven near-surface flow is of the opposite sign to \tilde{U}_{ex} and cannot drive near-surface offshore tracer transport here.

c. Submesoscale-flow induced cross-shore transport

The simulation snapshots (Fig. 3) show offshore propagating cross-shore elongated dye structures with a width of 0.6–3.8 km. In general, the MS–OS-boundary dye is patchy with subtidal dye alongshelf length scales $L_D^{(\text{MS,OS})}$ varying from 0.5 to 3 km (Figs. 5b,c), scales consistent with the coastal submesoscale (e.g., Dauhajre et al. 2017). Alongshelf surface density gradients are also consistently present at a variety of scales (Fig. 5a). The along-boundary perturbation dye transport Q'_x is a significant component of the total dye transport (Fig. 7b), particularly prior to 1 September. Here, we examine the role of submesoscale flows in driving along-boundary perturbation Q'_x via relationships between U'_{ex} [Eq. (9b)],

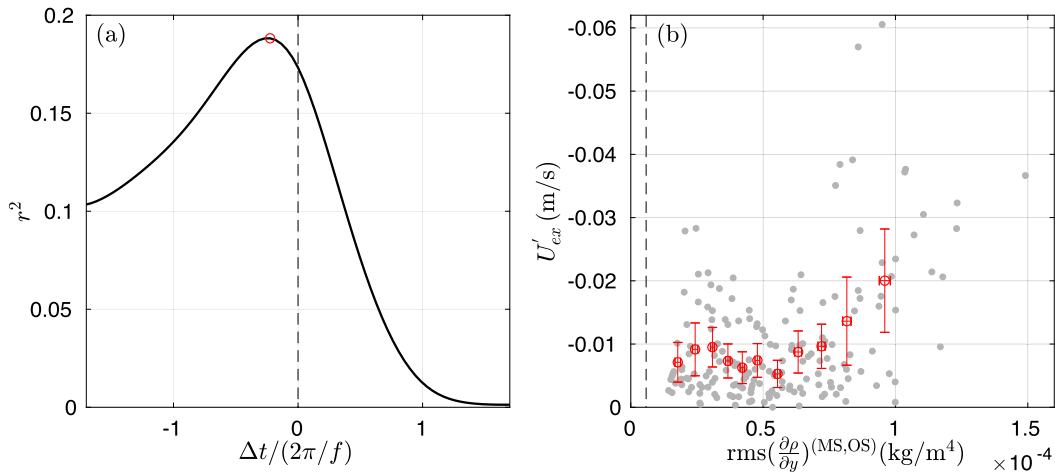


FIG. 11. (a) Lagged correlation between U'_{ex} and the alongshore rms alongshore density gradient $\text{rms}(\partial\rho/\partial y)^{(MS,OS)}$ vs inertial-period normalized time lag $\Delta t/(2\pi/f)$. Maximum correlation occurs when $\text{rms}(\partial\rho/\partial y)^{(MS,OS)}$ leads U'_{ex} by 0.22 inertial periods (red circle). (b) Scatterplot (gray) with binned means (red) of maximum r^2 time-lag-adjusted U'_{ex} vs $\text{rms}(\partial\rho/\partial y)^{(MS,OS)}$. The subtidal (and binned mean) square correlation is $r^2 = 0.19$ ($r^2 = 0.51, p < 0.05$). The dashed line in (b) denotes the MS–OS transition zone time-mean alongshore density gradient of $6 \times 10^{-6} \text{ kg m}^{-4}$.

the surface alongshelf dye length scale L_D [Eq. (11)], and the MS–OS boundary rms surface alongshelf density gradient $\text{rms}(\partial\rho/\partial y)^{(MS,OS)}$.

The subtidal exchange velocity U'_{ex} is more negative for smaller $L_D^{(MS,OS)}$ (Fig. 10) with binned-mean squared correlation of $r^2 = 0.32$ ($p < 0.05$). On average U'_{ex} is 2 times larger for $L_D^{(MS,OS)} < 0.9 \text{ km}$ than for $L_D^{(MS,OS)} > 1.2 \text{ km}$. The subtidal cross-boundary velocity length scale $L_u^{(MS,OS)}$ varies between 0.4 and 2 km and U'_{ex} is more negative for smaller $L_u^{(MS,OS)}$ (not shown). Overall, the stronger offshore U'_{ex} linked to smaller $L_D^{(MS,OS)}$ and $L_u^{(MS,OS)}$ suggests that the perturbation offshore dye transport Q'_x is largely due to relatively short ($< 2 \text{ km}$) length scales associated with submesoscale flows.

An along-boundary density gradient could induce a cross-MS–OS-boundary (i.e., alongfront) flow, and thus U'_{ex} , through geostrophic adjustment. As the density is time dependent (Fig. 5a), such cross-MS–OS-boundary flow must adjust and U'_{ex} would be elevated and time-lagged for stronger $\text{rms}(\partial\rho/\partial y)^{(MS,OS)}$. The time-lagged squared correlation r^2 between $\text{rms}(\partial\rho/\partial y)^{(MS,OS)}$ (Fig. 11a) has a maximum $r^2 = 0.19$ ($p > 0.05$) when $\text{rms}(\partial\rho/\partial y)^{(MS,OS)}$ leads U'_{ex} by 0.22 inertial periods (5 h). After adjusting for this time lag, U'_{ex} is consistently more negative for larger $\text{rms}(\partial\rho/\partial y)^{(MS,OS)}$ (Fig. 11b), with binned mean $r^2 = 0.51$ ($p < 0.05$), particularly for $\text{rms}(\partial\rho/\partial y)^{(MS,OS)} > 0.5 \times 10^{-4} \text{ kg m}^{-4}$. Using a scaled thermal wind relationship and assuming depth-uniform along-boundary density gradients (e.g., McWilliams 2016), a scaling for the

rms geostrophic cross-boundary velocity $\text{rms}(U_g)$ can be written as

$$\text{rms}(U_g)^{(MS,OS)} = \left(\frac{gd}{\rho_0 f} \right) \text{rms} \left(\frac{\partial\rho}{\partial y} \right)^{(MS,OS)}, \quad (13)$$

where d is the average vertical scale of the density gradient. Here, the rms density gradients are largely coherent over the upper 10 m of the water column (not shown) setting an average vertical scale of $d = 5 \text{ m}$ in the scaling [Eq. (13)]. With this, a subtidal $\text{rms}(\partial\rho/\partial y)^{(MS,OS)} = 0.5 \times 10^{-4} \text{ kg m}^{-4}$ yields a $\text{rms}(U_g)^{(MS,OS)} = 0.03 \text{ m s}^{-1}$, a factor 3 times larger than U'_{ex} , consistent with this process driving exchange. Note, U'_{ex} will be smaller than $(U_g)^{(MS,OS)}$ because frontal velocities are both onshore and offshore and recirculate dye. This indicates that when strong density gradients associated with $O(1) \text{ km}$ length scales are oriented alongshelf, cross-shore flows are induced with a time lag that transport dye offshore at these submesoscale length scales (Fig. 10). A model that does not adequately resolve these submesoscale flows will underestimate offshore tracer transport.

6. Discussion

a. Potential mechanism for rms alongshore density gradient generation

Several mechanisms have been posited for the generation of open-ocean submesoscale variability such as mixed layer instability (e.g., Boccaletti et al. 2007),

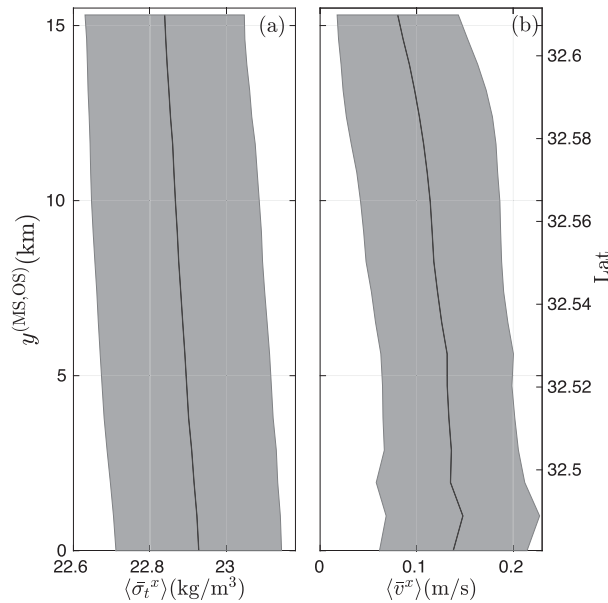


FIG. 12. (a) The temporal mean (black curve) and std (shading) of surface density anomaly $\langle \bar{\sigma}_t^x \rangle$ cross-shore averaged within the MS–OS transition zone, (b) the temporal mean and std of surface alongshelf subtidal current velocity for when $V_{SB} > 0$ ($\langle \bar{v}^x \rangle^{(>0)}$).

turbulent thermal wind balance (e.g., McWilliams et al. 2015), and deformation flow induced frontogenesis (e.g., Hoskins 1982). The presence of a shoreline boundary and shallow depths adds additional complexity. Here, we examine the role of an alongshore surface deformation flow in enhancing the existing mean alongshore density gradient potentially leading to the enhanced $\text{rms}(\partial\rho/\partial y)^{(\text{MS,OS})}$. Detailed diagnosis of the submesoscale variability and dynamics will occur elsewhere.

Density and alongshelf current statistics are time-averaged and cross-shore averaged within the MS–OS transition zone. The time-averaged and cross-shore averaged surface density $\langle \bar{\rho}^x \rangle$ has a quasi-linear time-mean alongshelf density gradient (Fig. 12a), consistent with the mean density distribution (Fig. 4a3). The average alongshelf density gradient $\partial\langle \bar{\rho}^x \rangle/\partial y = -6 \times 10^{-6} \text{ kg m}^{-4}$ is weaker by a factor 5–30 times than $\text{rms}(\partial\rho/\partial y)^{(\text{MS,OS})}$ (Fig. 11b). During the analysis period, the subtidal V_{SB} is mostly northward (Fig. 2f). The surface alongshelf velocity is first cross-shore averaged within MS–OS transition zone and then time-averaged when $V_{SB} > 0$ yielding $\langle \bar{v}^x \rangle^{(>0)}(y)$, which has a consistent negative alongshelf gradient (Fig. 12b), indicating alongshelf convergence, likely due to the regional bathymetry. A linear best fit yields a $\partial\langle \bar{v}^x \rangle^{(>0)}/\partial y = -3.8 \times 10^{-6} \text{ s}^{-1}$, 2–5 times larger than the normal strain rate of mesoscale eddies (e.g., Chaigneau et al. 2008). If this northward convergent flow was responsible for strengthening

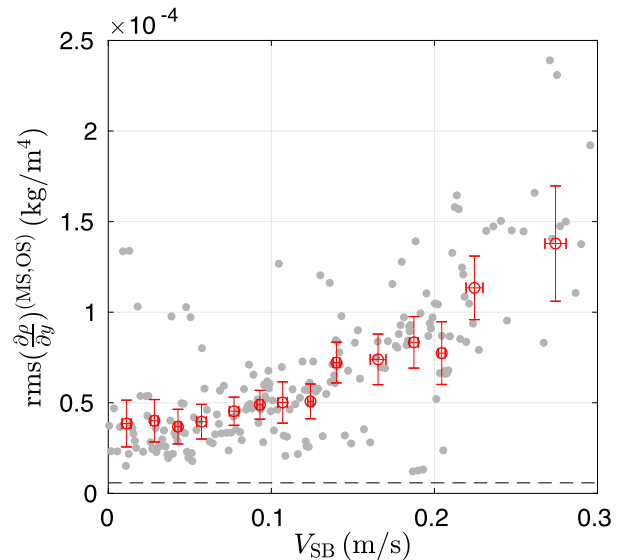


FIG. 13. The MS–OS boundary rms alongshore density gradient $\text{rms}(\partial\rho/\partial y)^{(\text{MS,OS})}$ vs the depth-averaged subtidal alongshore velocity at SB V_{SB} . All values are subtidally filtered, gray points are shown only every 8 h, and the binned means have 120-h points each. The subtidal (and binned mean) squared correlations are $r^2 = 0.49$ ($r^2 = 0.88$). The horizontal dashed line is the MS–OS transition zone time-mean density gradient of $6 \times 10^{-6} \text{ kg m}^{-4}$.

$\text{rms}(\partial\rho/\partial y)^{(\text{MS,OS})}$, then a stronger $\text{rms}(\partial\rho/\partial y)^{(\text{MS,OS})}$ with increasing V_{SB} would be expected. Indeed, the subtidal $\text{rms}(\partial\rho/\partial y)^{(\text{MS,OS})}$ is consistently enhanced for stronger northward V_{SB} (Fig. 13) with $r^2 = 0.49$ ($p < 0.05$) and binned mean $r^2 = 0.88$ ($p < 0.05$). This fit does not change if only times when U_{ex}^i could be calculated (dashed line in Fig. 7a) are used in the fit. This indicates a linkage between the two processes and supports the concept that an alongshelf convergent flow is promoting generation of rms alongshelf density gradients.

b. Role of other mechanisms in offshore dye transport

Although wind-driven Ekman transport and along-front submesoscale flows were diagnosed as principal drivers of MS–OS boundary offshore tracer transport, the region is complex and other mechanisms may play a role. The stratification and circulation on subtidal time scales can be modified by BT (e.g., Ganju et al. 2011) and BC (Suanda et al. 2017) tides. Shelf BC tides enhanced 3D and 2D horizontal dispersion relative to simulations without BC tides (Suanda et al. 2018). Although DU BC tides did not principally drive subtidal offshore dye transport through a tidal exchange mechanism, BC tides could be similarly enhancing offshore transport relative to a no BC tide simulation (not performed). The TJRE shoal and large-scale bathymetry (coastline curvature, SDB entrance, and Pt. Loma) could also have a secondary

effect on the MS–OS offshore dye transport. For example, enhanced $\text{rms}(\zeta/f)$ (well above 1) and $|\nabla_{HP}\rho|$ variability at both the SDB entrance and the TJRE shoal (Figs. 4a5,b5) suggests strong local vorticity and buoyancy gradient generation. The surfzone also has strongly elevated vorticity and $|\nabla_{HP}\rho|$ variability relative to the MS–OS transition zone (Fig. 4). Although bathymetric rip currents are present here, transient rip current (TRC) forcing is not included in this model. However, TRCs also drive further enhanced vorticity (Johnson and Pattiaratchi 2006; Suanda and Feddersen 2015) and buoyancy gradient (Kumar and Feddersen 2017a,b) variability on alongshore length scales of 50–500 m (Hally-Rosendahl et al. 2014, 2015; Kumar and Feddersen 2017b). As the NS and regions farther offshore are material transport linked (as evidenced by dye), offshore transport of NS or TJRE shoal vorticity and $|\nabla_{HP}\rho|$ may seed submesoscale variability on the inner shelf and farther offshore, although of course neither is a conserved passive tracer. Although relatively weak, the freshwater sources at TJRE, Pt. Bandera, and within SDB could be an additional density gradient source.

Last, we examine the role of horizontal mixing in potentially inhibiting submesoscale variability generation. A horizontal eddy viscosity of $\nu_h = 0.5 \text{ m}^2 \text{ s}^{-1}$, 1-km length scale, and 0.1 m s^{-1} velocity scale give a horizontal Reynolds number of 200, indicating a priori weak horizontal mixing. Surface momentum balance terms calculated at the MS–OS boundary have rms horizontal mixing at ≈ 17 times and ≈ 23 times weaker than the vertical mixing and nonlinear advective terms, respectively. Thus, the horizontal mixing has a minor effect on submesoscale variability. A similar conclusion was drawn for turbulent-thermal wind filament frontogenesis from simulations with a similar grid resolution (12.5 m versus a mean of 20–30 m within the MS–OS transition zone) using both $\nu_h = 0.5 \text{ m}^2 \text{ s}^{-1}$ and $\nu_h = 0 \text{ m}^2 \text{ s}^{-1}$ (McWilliams et al. 2015).

c. Relative roles of transport terms and key parameters with implications for coastal water quality

Cross-shore transport has direct implications on shoreline water quality by diluting shoreline concentrations. For nonzero cross-MS–OS-boundary dye transport, PB shoreline-released dye must be present at the MS–OS boundary, requiring first northward NS transport driven by waves incident from the south ($S_{xy} > 0$, Fig. 2e). The baroclinic cross-MS–OS-boundary transport \tilde{Q}_x is linked to the wind-driven Ekman transport. Although relatively small, near-surface Ekman velocities were directed offshore for extended durations (Figs. 6a3 and 9d). Together with the surface enhanced dye, this

resulted in significant MS–OS-boundary dye transport with exchange velocity \tilde{U}_{ex} magnitude similar to the Ekman velocity. The along-boundary perturbation transport Q'_x [Eq. (8c)] is linked to increased boundary $\text{rms}(\partial\rho/\partial y)^{(MS,OS)}$ through alongfront geostrophic flow. Although the submesoscale velocities u' (Fig. 6b3) are as large as the \tilde{u} velocities, because the u' flows fluctuate onshore and offshore, significant recirculation is likely present and the resulting MS–OS-boundary U'_{ex} is substantially weaker than the rms velocities [Eq. (13) and Fig. 11b]. For the regional geography south of Pt. Loma, the $\text{rms}(\partial\rho/\partial y)^{(MS,OS)}$ is enhanced during northward convergent mean flow, primarily APG driven (Fig. 8), allowing diagnosis of $\text{rms}(\partial\rho/\partial y)^{(MS,OS)}$ from V_{SB} . Thus, for a shoreline-released tracer, the key parameters cross-MS–OS-boundary transport are S_{xy} , alongshelf winds, and V_{SB} . Other headland bounded regions may be similar.

During the analysis period, S_{xy}/ρ_0 is mostly positive (Fig. 2e) and V_{SB} is largely northward with only a few short times of southward flow (Fig. 2f). The winds are mostly upwelling favorable, with only a few cases of sustained downwelling favorable conditions (10–12 September and 4–6 October, Fig. 2c). The 4–6 October downwelling winds occur during negative to weak positive S_{xy} , and thus relatively little dye is present in both the NS and at the MS–OS boundary (Fig. 7a). The 10–12 September downwelling wind conditions are interesting because S_{xy} was strongly positive leading to strongly elevated $\bar{D}^{(NS)} > 10^{-3}$ (Fig. 7a) and shelf flow was also strongly northward ($V_{SB} > 0.2 \text{ m s}^{-1}$, Fig. 2f), but had the weakest MS–OS boundary dye, mostly $< 10^{-6}$ (Fig. 7a).

To explain the lack of MS–OS boundary dye, we examine this 10–12 September event with two model snapshots spanning 57 h (Fig. 14). At the event start (0100 UTC 10 September), shoreline-released dye streams north remaining mostly within the 500-m-wide NS, before the flow separates near 32.63°N , bends around Pt. Loma, and continues north (Fig. 14a). Toward the end of the event (1000 UTC 12 September), dye is still concentrated in the 500-m-wide NS, but there are ≈ 1 km alongshore scale plume structures extending 1–3 km offshore, and, farther north, the dye plume wraps around Pt. Loma (Fig. 14b). In both cases, the $D = 10^{-4}$ contour is always at > 2 km from the MS–OS boundary. For the entire event duration, MS–OS boundary never had $D \geq 10^{-5}$ (Fig. 5b, cyan rectangle). During this event, winds were only moderately northward (Fig. 2c), yet the MS–OS-boundary surface \tilde{u} was onshore at roughly 0.05 m s^{-1} for many days. This is likely due to onshore surface Ekman transport but may also be enhanced by onshore flow balancing offshore bottom

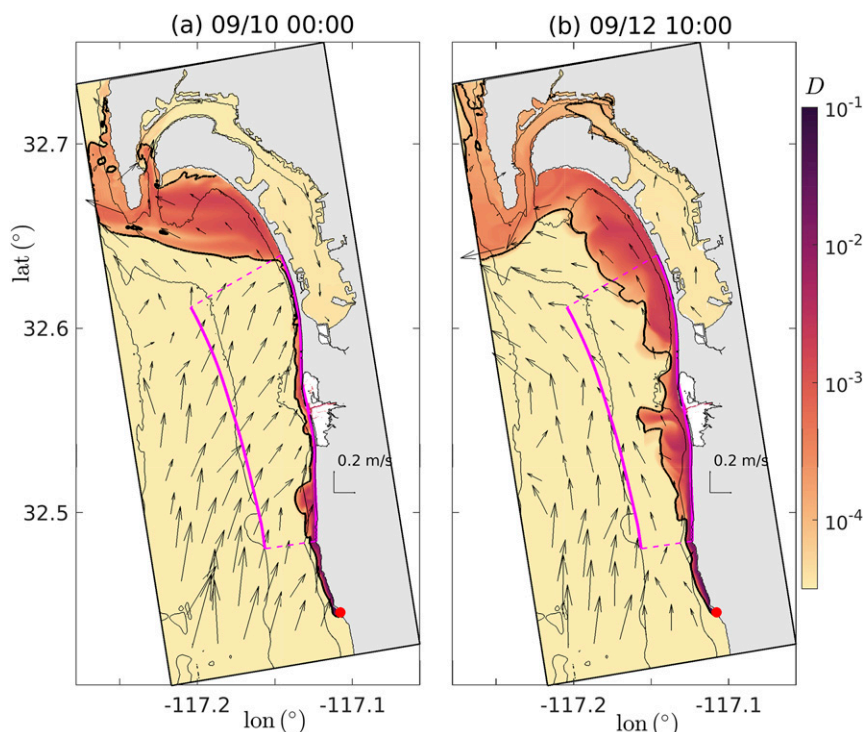


FIG. 14. Two surface dye (color) and surface current velocity (arrows) snapshots during strong northward wave-driven flow and downwelling winds spanning 58 h: (a) 0100 UTC 10 Sep and (b) 1000 UTC 12 Sep. Thin lines show bathymetry contours at $h = [10, 25, 45]$ m. The magenta curves outline the NS and MS–OS boundaries. The thick black line represents the $D = 10^{-4}$ contour. The red dot denotes the PB source.

Ekman transport from the northward APG-driven flow. In conclusion, both SZ and shelf processes influence shoreline concentrations for shoreline-released tracers. Simultaneously occurring northward surfzone currents, downwelling winds, and northward forcing APG, (e.g., 10–12 September) is the worst-case scenario for regional beach water quality, as offshore transport from the NS is weak, and the shoreline is not diluted.

7. Summary

Here, we investigate the processes transporting a shoreline-released dye representing untreated wastewater in the San Diego–Tijuana region that has a curving shoreline, an estuary, a bay, and a headland. A high-resolution wave–current coupled model is used resolving the surfzone and receiving realistic air–sea forcing, tides, waves, and offshore boundary conditions inherited from a larger-scale data assimilated model. Model dye is shoreline released 10 km south of the U.S.–Mexico border representing untreated wastewater and analyzed from midsummer to fall with largely southerly incident waves, mostly northward alongshelf flow, strong shelf stratification, and moderate wind forcing. Analysis

focuses primarily on the tracer transport across the midshelf (MS) to outer-shelf (OS) boundary (≈ 25 -m depth) chosen as a streamline of the time mean and depth-averaged velocity.

Within 500 m of the shoreline, alongshore tracer transport is primarily driven by obliquely incident wave breaking. At the MS–OS boundary, alongshore density gradients are persistent and dye is surface enhanced and time and alongshore patchy with length scales from 0.3 to 4 km. Significant vertical (baroclinic) and along-boundary density and velocity variability is present. The cross-MS–OS-boundary dye transport has significant baroclinic and along-boundary perturbation components from which baroclinic and along-boundary perturbation dye exchange velocities are estimated. Barotropic tides and semidiurnal baroclinic tides cannot explain these two exchange velocity components. The baroclinic exchange velocity is significantly correlated and has similar magnitude to a simply Ekman transport velocity, indicating Ekman transport is driving the baroclinic cross-MS–OS-boundary tracer transport. The perturbation exchange velocity is elevated for smaller (< 1 km) alongshore dye length scales and stronger root-mean-square (rms) alongshore density

gradients $\partial\rho/\partial y$, indicating geostrophic along-frontal submesoscale flows induce the along-MS–OS-boundary perturbation transport. During periods of northward flows, the surface alongshore current is convergent with a relatively strong mean deformation rate. Stronger northward flows are linked to elevated $\text{rms}(\partial\rho/\partial y)^{(\text{MS,OS})}$, potentially generated by deformation frontogenesis. A model that does not adequately resolve these submesoscale flows will underestimate offshore tracer transport. Both surfzone and shelf processes influence offshore transport for shoreline-released tracers, and the key parameters governing cross-MS–OS-boundary dye transport are the incident S_{xy} , the alongshelf winds, and the APG-driven alongshelf current. When the co-occurrence of these parameters strongly inhibits offshore transport, shoreline concentrations are not effectively diluted leading to poor water quality.

Acknowledgments. This work was supported by the National Science Foundation (OCE-1459389) as part of the Cross-Surfzone/Inner-shelf Dye Exchange (CSIDE) experiment. Additional funding is through the Environmental Protection Agency through the North American Development Bank, however, it does not necessarily reflect the policies, actions or positions of the U.S. EPA or NADB. NK was supported by ONR Award N00014-17-1-2890 and NSF Award OCE-1735460. ONR supported GG via NOPP Award N000141512598. The numerical simulations were performed on the comet cluster at the San Diego Super Computer Center through the Extreme Science and Engineering Discovery Environment (XSEDE), which is supported by National Science Foundation (ACI-1548562). NOAA provided the NAM atmospheric forcing fields and the bathymetries. SIO Coastal Data Information Program provided wave forcing. Chris Edwards from UC Santa Cruz provided COAMPS data generated by NRL. We also appreciate extra support from the Tijuana River National Estuarine Research Reserve, the Southern California Coastal Ocean Observing System. CASE solutions are available online (<http://ecco.ucsd.edu/case.html>) Geno Pawlak, Derek Grimes, Andre Amador, and Bruce Cornuelle provided useful feedback to this work. We appreciate insight from Jack McSweeney.

APPENDIX

Barotropic and Baroclinic Tide Surface Velocity Amplitude Estimation

Here, the MS–OS boundary barotropic and surface baroclinic tidal velocities estimation method is described. The cross-shore velocity is first decomposed

into barotropic (BT, depth averaged) and baroclinic (BC) components along the boundary. These two components are then bandpass filtered to obtain the semi-diurnal (SD, 16^{-1} to 10^{-1} cph) and diurnal (DU, 33^{-1} to 16^{-1} cph) band components. Here, the SD-band analysis is described. First, we calculate the bulk BT SD tidal velocity amplitude (envelope) (U_{SD}), assumed narrow banded with form

$$U_{\text{SD}}(t, y) = \hat{U}_{\text{SD}}(\epsilon t, y) \cos(2\pi\omega_{\text{SD}}t + \theta_{\text{SD}}), \quad (\text{A1})$$

where ω_{SD} is the SD frequency, \hat{U}_{SD} is the SD velocity amplitude that varies on longer time scale (denoted as ϵt), and θ_{SD} is a phase that will only vary slightly over the MS–OS boundary. As the BT tidal velocity is narrow banded, the amplitude \hat{U}_{SD} is estimated via Hilbert transform at each alongshore location. The alongshore mean and std are presented in Fig. 9b.

BC velocities vary with depth and have much shorter length scales than the BT tidal velocities, leading to additional analysis. At each location y_i along the MS–OS boundary, the SD baroclinic cross-shore current $u_{\text{SD}}(y_i, z, t)$ is decomposed into a vertical EOF such that

$$u_{\text{SD}}(y_i, z, t) = \sum_{n=1}^N I_{\text{SD}}^{(n)}(y_i, t) \Phi_{\text{SD}}^{(n)}(y_i, z), \quad (\text{A2})$$

where $I_{\text{SD}}^{(n)}(t)$ and $\Phi_{\text{SD}}^{(n)}(z)$ are the EOF amplitude and vertical structure at y_i , and $N = 15$ is the total number of vertical levels. At all MS–OS boundary locations, the first ($n = 1$) EOF accounts for >78% of the SD-band variance (>92% of the DU-band variance). For both bands, the first vertical EOF [$\Phi_{\text{SD}}^{(1)}(z)$ and $\Phi_{\text{DU}}^{(1)}(z)$] is consistent with a first-mode baroclinic motions with midwater column sign change and is nearly alongshore uniform on the MS–OS boundary (Fig. A1a). Thus, surface BC tidal cross-shore velocities can be reconstructed with a single EOF at all alongshore locations, i.e., for the SD-band surface velocity

$$u_{\text{SD}}^{(1)}(y, \eta, t) = I_{\text{SD}}^{(1)}(y, t) \Phi_{\text{SD}}^{(1)}(y, \eta).$$

The alongshore coherent variability of reconstructed surface SD cross-shore velocity $u_{\text{SD}}^{(1)}(y, \eta, t)$ [and also DU $u_{\text{DU}}^{(1)}(y, \eta, t)$] is further examined with a complex (Hilbert) EOF (CEOF) (e.g., Horel 1984; Merrifield and Guza 1990). A complex time series is generated according to

$$u_{*\text{SD}}^{(1)}(y, t) = u_{\text{SD}}^{(1)}(y, t) + i\tilde{u}_{\text{SD}}^{(1)}(y, t), \quad (\text{A3})$$

where \tilde{u}_{SD} is the Hilbert transform of u_{SD} and $i = \sqrt{-1}$. The variability of $u_{*\text{SD}}^{(1)}(y, t)$ is then CEOF decomposed into

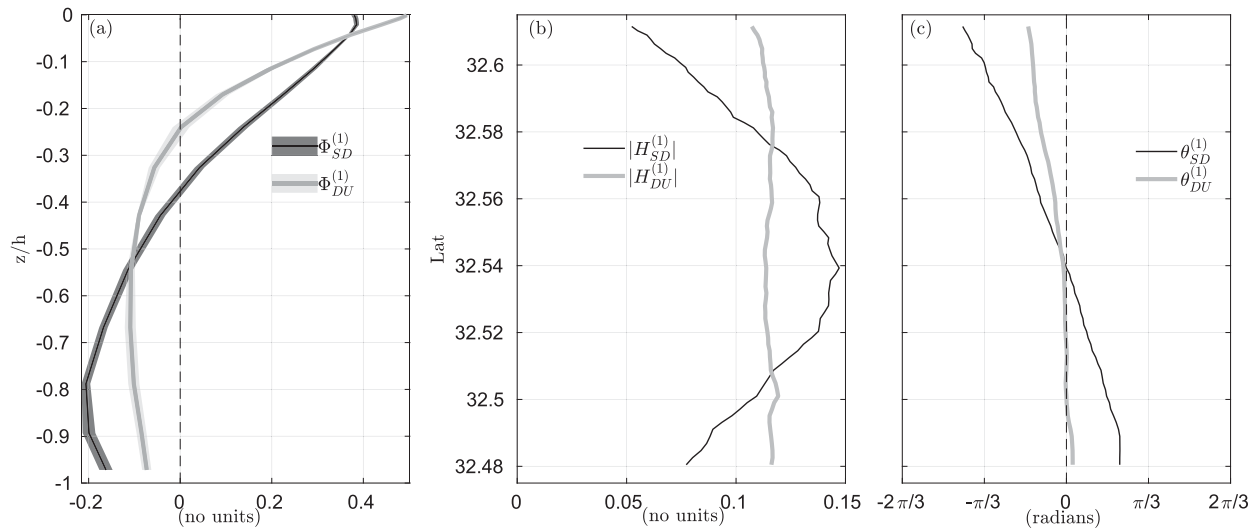


FIG. A1. (a) Vertical profile of the first EOF of the SD and DU band cross-shore current velocity. The alongshelf variation on the MS–OS boundary of the (b) amplitude ($|H_{SD}^{(1)}|$, $|H_{DU}^{(1)}|$) and (c) phase ($\theta_{SD}^{(1)}$, $\theta_{DU}^{(1)}$) of the first CEOF of $u_{SD}^{(1)}$ and $u_{DU}^{(1)}$, respectively.

$$u_{*SD}^{(1)}(y, t) = \sum_{n=1}^M B_{SD}^{(n)}(t) H_{SD}^{(n)}(y), \quad (\text{A4})$$

where M is the total number of MS–OS boundary grid points, $H_{SD}^{(n)}(y)$ is the complex eigenvector, and $B_{SD}^{(n)}(t)$ is the complex amplitude.

The alongshore first CEOF of the SD and DU band explains 56% and 95% of the alongshore variability, respectively. The magnitude of the SD $|H_{SD}^{(1)}(y)|$ is maximum near the center of the MS–OS boundary, and is reduced about 50% at the northern and southern ends (Fig. A1b). The DU $|H_{SD}^{(1)}(y)|$ is largely alongshore uniform (Fig. A1b). The SD along boundary phase is estimated as

$$\theta_{SD}^{(1)}(y) = \text{atan} \left\{ \frac{\Im[H_{SD}^{(1)}(y)]}{\Re[H_{SD}^{(1)}(y)]} \right\}, \quad (\text{A5})$$

where \Im and \Re are the imaginary and real operators, respectively. For the SD band, the phase $\theta_{SD}^{(1)}(y)$ varies quasi-linearly by $\pi/2$ (90°) along the 15-km boundary (Fig. A1c), suggesting southward propagation of the SD BC tide. For the DU band, the phase is near zero for the southern half of the boundary, and varies $\pi/6$ (30°) over the northern half (Fig. A1c), also indicating mostly southward propagation, consistent with the regional observations of southward DU-band propagation in 12–15-m depth (Grimes et al. 2020). Overall, the phase variations indicate that the SD and DU BC tides alongshelf scale is substantially larger than the 15-km length of the MS–OS boundary. The amplitude of the first CEOF reconstructed SD and DU surface velocities are estimated as for the BT tidal velocity at each y location

resulting in surface $\hat{u}_{SD}^{(1)}(y, \epsilon t)$ and $\hat{u}_{DU}^{(1)}(y, \epsilon t)$. The alongshore mean and std are shown in Fig. 9c and described in section 5a.

REFERENCES

- Ahn, J. H., S. B. Grant, C. Q. Surbeck, P. M. DiGiacomo, N. P. Nezlin, and S. Jiang, 2005: Coastal water quality impact of stormwater runoff from an urban watershed in southern California. *Environ. Sci. Technol.*, **39**, 5940–5953, <https://doi.org/10.1021/es0501464>.
- Archfield, S. A., and R. M. Vogel, 2010: Map correlation method: Selection of a reference streamgage to estimate daily streamflow at ungaged catchments. *Water Resour. Res.*, **46**, W10513, <https://doi.org/10.1029/2009WR008481>.
- Austin, J. A., and S. J. Lentz, 2002: The inner shelf response to wind-driven upwelling and downwelling. *J. Phys. Oceanogr.*, **32**, 2171–2193, [https://doi.org/10.1175/1520-0485\(2002\)032<2171:TISRTW>2.0.CO;2](https://doi.org/10.1175/1520-0485(2002)032<2171:TISRTW>2.0.CO;2).
- Becker, B. J., L. A. Levin, F. J. Fodrie, and P. A. McMillan, 2007: Complex larval connectivity patterns among marine invertebrate populations. *Proc. Natl. Acad. Sci. USA*, **104**, 3267–3272, <https://doi.org/10.1073/pnas.0611651104>.
- Boccaletti, G., R. Ferrari, and B. Fox-Kemper, 2007: Mixed layer instabilities and restratification. *J. Phys. Oceanogr.*, **37**, 2228–2250, <https://doi.org/10.1175/JPO3101.1>.
- Booij, N., R. C. Ris, and L. H. Holthuijsen, 1999: A third-generation wave model for coastal regions: 1. Model description and validation. *J. Geophys. Res.*, **104**, 7649–7666, <https://doi.org/10.1029/98JC02622>.
- Brown, J. A., J. H. MacMahan, A. J. H. M. Reniers, and E. B. Thornton, 2015: Field observations of surf zone–inner shelf exchange on a rip-channeled beach. *J. Phys. Oceanogr.*, **45**, 2339–2355, <https://doi.org/10.1175/JPO-D-14-0118.1>.
- Buijsman, M., Y. Uchiyama, J. McWilliams, and C. Hill-Lindsay, 2012: Modeling semidiurnal internal tide variability in the Southern California bight. *J. Phys. Oceanogr.*, **42**, 62–77, <https://doi.org/10.1175/2011JPO4597.1>.

- Castelao, R. M., and J. A. Barth, 2006: The relative importance of wind strength and along-shelf bathymetric variations on the separation of a coastal upwelling jet. *J. Phys. Oceanogr.*, **36**, 412–425, <https://doi.org/10.1175/JPO2867.1>.
- Castelle, B., and G. Coco, 2013: Surf zone flushing on embayed beaches. *Geophys. Res. Lett.*, **40**, 2206–2210, <https://doi.org/10.1002/grl.50485>.
- Chadwick, D. B., and J. L. Largier, 1999: Tidal exchange at the bay-ocean boundary. *J. Geophys. Res.*, **104**, 29 901–29 924, <https://doi.org/10.1029/1999JC900165>.
- Chaigneau, A., A. Gizolme, and C. Grados, 2008: Mesoscale eddies off Peru in altimeter records: Identification algorithms and eddy spatio-temporal patterns. *Prog. Oceanogr.*, **79**, 106–119, <https://doi.org/10.1016/j.pocean.2008.10.013>.
- Chapman, D. C., 1985: Numerical treatment of cross-shelf open boundaries in a barotropic coastal ocean model. *J. Phys. Oceanogr.*, **15**, 1060–1075, [https://doi.org/10.1175/1520-0485\(1985\)015<1060:NTOCSO>2.0.CO;2](https://doi.org/10.1175/1520-0485(1985)015<1060:NTOCSO>2.0.CO;2).
- Dauhajre, D. P., and J. C. McWilliams, 2019: Nearshore Lagrangian connectivity: Submesoscale influence and resolution sensitivity. *J. Geophys. Res. Oceans*, **124**, 5180–5204, <https://doi.org/10.1029/2019JC014943>.
- , —, and Y. Uchiyama, 2017: Submesoscale coherent structures on the continental shelf. *J. Phys. Oceanogr.*, **47**, 2949–2976, <https://doi.org/10.1175/JPO-D-16-0270.1>.
- Ekman, V. W., 1905: On the influence of the Earth's rotation on ocean currents. *Ark. Mat. Astron. Fys.*, **2**, 1–52.
- Estrade, P., P. Marchesiello, D. Verdière, A. Colin, and C. Roy, 2008: Cross-shelf structure of coastal upwelling: A two-dimensional extension of Ekman's theory and a mechanism for inner shelf upwelling shut down. *J. Mar. Res.*, **66**, 589–616, <https://doi.org/10.1357/002224008787536790>.
- Feddersen, F., 2012: Scaling surf zone turbulence. *Geophys. Res. Lett.*, **39**, L18613, <https://doi.org/10.1029/2012GL052970>.
- , 2014: The generation of surfzone eddies in a strong along-shore current. *J. Phys. Oceanogr.*, **44**, 600–617, <https://doi.org/10.1175/JPO-D-13-051.1>.
- , R. Guza, S. Elgar, and T. Herbers, 1998: Alongshore momentum balances in the nearshore. *J. Geophys. Res.*, **103**, 15 667–15 676, <https://doi.org/10.1029/98JC01270>.
- , M. Olabarrieta, R. T. Guza, D. Winters, B. Raubenheimer, and S. Elgar, 2016: Observations and modeling of a tidal inlet dye tracer plume. *J. Geophys. Res. Oceans*, **121**, 7819–7844, <https://doi.org/10.1002/2016JC011922>.
- Fewings, M., S. J. Lentz, and J. Fredericks, 2008: Observations of cross-shelf flow driven by cross-shelf winds on the inner continental shelf. *J. Phys. Oceanogr.*, **38**, 2358–2378, <https://doi.org/10.1175/2008JPO3990.1>.
- Flather, R., 1976: A tidal model of the north-west European continental shelf. *Mem. Soc. Roy. Sci. Liege.*, **10**, 141–164.
- Gan, J., and J. S. Allen, 2002: A modeling study of shelf circulation off Northern California in the region of the coastal ocean dynamics experiment: Response to relaxation of upwelling winds. *J. Geophys. Res.*, **107**, 3123, <https://doi.org/10.1029/2000JC000768>.
- Ganju, N. K., S. J. Lentz, A. R. Kirincich, and J. T. Farrar, 2011: Complex mean circulation over the inner shelf south of Martha's Vineyard revealed by observations and a high-resolution model. *J. Geophys. Res.*, **116**, C10036, <https://doi.org/10.1029/2011JC007035>.
- Geyer, W. R., and P. MacCready, 2014: The estuarine circulation. *Annu. Rev. Fluid Mech.*, **46**, 175–197, <https://doi.org/10.1146/annurev-fluid-010313-141302>.
- Giddings, S. N., and Coauthors, 2014: Hindcasts of potential harmful algal bloom transport pathways on the Pacific Northwest coast. *J. Geophys. Res. Oceans*, **119**, 2439–2461, <https://doi.org/10.1002/2013JC009622>.
- Grant, S. B., J. H. Kim, B. H. Jones, S. A. Jenkins, J. Wasyl, and C. Cudaback, 2005: Surf zone entrainment, along-shore transport, and human health implications of pollution from tidal outlets. *J. Geophys. Res.*, **110**, C10025, <https://doi.org/10.1029/2004JC002401>.
- Grimes, D. J., F. Feddersen, S. N. Giddings, and G. Pawlak, 2020: Cross-shore deformation of a surfzone-released dye plume by an internal tide on the inner shelf. *J. Phys. Oceanogr.*, **50**, 35–54, <https://doi.org/10.1175/JPO-D-19-0046.1>.
- Hally-Rosendahl, K., and F. Feddersen, 2016: Modeling surfzone to inner-shelf tracer exchange. *J. Geophys. Res. Oceans*, **121**, 4007–4025, <https://doi.org/10.1002/2015JC011530>.
- , —, and R. Guza, 2014: Cross-shore tracer exchange between the surfzone and inner-shelf. *J. Geophys. Res. Oceans*, **119**, 4367–4388, <https://doi.org/10.1002/2013JC009722>.
- , —, D. B. Clark, and R. T. Guza, 2015: Surfzone to inner-shelf exchange estimated from dye tracer balances. *J. Geophys. Res. Oceans*, 6289–6308, <https://doi.org/10.1002/2015jc010844>.
- Hickey, B., E. L. Dobbins, and S. E. Allen, 2003: Local and remote forcing of currents and temperature in the central Southern California bight. *J. Geophys. Res.*, **108**, 3081, <https://doi.org/10.1029/2000JC000313>.
- Horel, J. D., 1984: Complex principal component analysis: Theory and examples. *J. Climate Appl. Meteor.*, **23**, 1660–1673, [https://doi.org/10.1175/1520-0450\(1984\)023<1660:CPCATA>2.0.CO;2](https://doi.org/10.1175/1520-0450(1984)023<1660:CPCATA>2.0.CO;2).
- Horwitz, R. M., and S. J. Lentz, 2016: The effect of wind direction on cross-shelf transport on an initially stratified inner shelf. *J. Mar. Res.*, **74**, 201–227, <https://doi.org/10.1357/002224016820870648>.
- Hoskins, B., 1982: The mathematical theory of frontogenesis. *Annu. Rev. Fluid Mech.*, **14**, 131–151, <https://doi.org/10.1146/annurev.fl.14.010182.001023>.
- Johnson, D., and C. Pattiaratchi, 2006: Boussinesq modelling of transient rip currents. *Coast. Eng.*, **53**, 419–439, <https://doi.org/10.1016/j.coastaleng.2005.11.005>.
- Johnston, T. S., and D. L. Rudnick, 2015: Trapped diurnal internal tides, propagating semidiurnal internal tides, and mixing estimates in the California current system from sustained glider observations, 2006–2012. *Deep-Sea Res. II*, **112**, 61–78, <https://doi.org/10.1016/j.dsr2.2014.03.009>.
- Kim, S. Y., 2010: Observations of submesoscale eddies using high-frequency radar-derived kinematic and dynamic quantities. *Cont. Shelf Res.*, **30**, 1639–1655, <https://doi.org/10.1016/j.csr.2010.06.011>.
- , E. J. Terrill, and B. D. Cornuelle, 2009: Assessing coastal plumes in a region of multiple discharges: The US-Mexico border. *Environ. Sci. Technol.*, **43**, 7450–7457, <https://doi.org/10.1021/es900775p>.
- , B. D. Cornuelle, and E. J. Terrill, 2010: Decomposing observations of high-frequency radar-derived surface currents by their forcing mechanisms: Decomposition techniques and spatial structures of decomposed surface currents. *J. Geophys. Res.*, **115**, C12007, <https://doi.org/10.1029/2010JC006222>.
- , and Coauthors, 2011: Mapping the U.S. west coast surface circulation: A multiyear analysis of high-frequency radar observations. *J. Geophys. Res.*, **116**, C03011, <https://doi.org/10.1029/2010JC006669>.
- Kumar, N., and F. Feddersen, 2017a: The effect of Stokes drift and transient rip currents on the inner shelf. Part II: With stratification. *J. Phys. Oceanogr.*, **47**, 243–260, <https://doi.org/10.1175/JPO-D-16-0077.1>.
- , and —, 2017b: A new offshore transport mechanism for shoreline-released tracer induced by transient rip currents

- and stratification. *Geophys. Res. Lett.*, **44**, 2843–2851, <https://doi.org/10.1002/2017GL072611>.
- , G. Voulgaris, J. C. Warner, and M. Olabarrieta, 2012: Implementation of the vortex force formalism in the coupled ocean-atmosphere-wave-sediment transport (COAWST) modeling system for inner shelf and surf zone applications. *Ocean Modell.*, **47**, 65–95, <https://doi.org/10.1016/j.ocemod.2012.01.003>.
- , F. Feddersen, Y. Uchiyama, J. McWilliams, and W. O. Reilly, 2015: Midshelf to surfzone coupled ROMS–SWAN model data comparison of waves, currents, and temperature: Diagnosis of subtidal forcings and response. *J. Phys. Oceanogr.*, **45**, 1464–1490, <https://doi.org/10.1175/JPO-D-14-0151.1>.
- , —, S. Suanda, Y. Uchiyama, and J. McWilliams, 2016: Mid- to inner-shelf coupled ROMS–SWAN model-data comparison of currents and temperature: Diurnal and semidiurnal variability. *J. Phys. Oceanogr.*, **46**, 841–862, <https://doi.org/10.1175/JPO-D-15-0103.1>.
- , S. H. Suanda, J. A. Colosi, K. Haas, E. Di Lorenzo, A. J. Miller, and C. A. Edwards, 2019: Coastal semidiurnal internal tidal incoherence in the Santa Maria basin, California: Observations and model simulations. *J. Geophys. Res. Oceans*, **124**, 5158–5179, <https://doi.org/10.1029/2018JC014891>.
- Lentz, S. J., 2008: Observations and a model of the mean circulation over the middle Atlantic bight continental shelf. *J. Phys. Oceanogr.*, **38**, 1203–1221, <https://doi.org/10.1175/2007JPO3768.1>.
- , and C. D. Winant, 1986: Subinertial currents on the Southern California shelf. *J. Phys. Oceanogr.*, **16**, 1737–1750, [https://doi.org/10.1175/1520-0485\(1986\)016<1737:SCOTSC>2.0.CO;2](https://doi.org/10.1175/1520-0485(1986)016<1737:SCOTSC>2.0.CO;2).
- , and M. R. Fewings, 2012: The wind- and wave-driven inner-shelf circulation. *Annu. Rev. Mar. Sci.*, **4**, 317–343, <https://doi.org/10.1146/annurev-marine-120709-142745>.
- , R. T. Guza, S. Elgar, F. Feddersen, and T. H. C. Herbers, 1999: Momentum balances on the North Carolina inner shelf. *J. Geophys. Res.*, **104**, 18 205–18 226, <https://doi.org/10.1029/1999JC900101>.
- Lerczak, J. A., M. Hendershott, and C. Winant, 2001: Observations and modeling of coastal internal waves driven by a diurnal sea breeze. *J. Geophys. Res.*, **106**, 19 715–19 729, <https://doi.org/10.1029/2001JC000811>.
- , C. D. Winant, and M. C. Hendershott, 2003: Observations of the semidiurnal internal tide on the southern California slope and shelf. *J. Geophys. Res.*, **108**, 3068, <https://doi.org/10.1029/2001JC001128>.
- , W. R. Geyer, and R. J. Chant, 2006: Mechanisms driving the time-dependent salt flux in a partially stratified estuary. *J. Phys. Oceanogr.*, **36**, 2296–2311, <https://doi.org/10.1175/JPO2959.1>.
- Limeburner, R., and Coauthors, 1985: CODE-2: Moored array and large-scale data report. WHOI Tech. Rep 85-35, CODE Tech. Rep. 38, Woods Hole Oceanographic Institution, 242 pp.
- Longuet-Higgins, M. S., 1970: Longshore currents generated by obliquely incident sea waves: 1. *J. Geophys. Res.*, **75**, 6778–6789, <https://doi.org/10.1029/JC075i033p06778>.
- Marchesiello, P., and P. Estrade, 2010: Upwelling limitation by onshore geostrophic flow. *J. Mar. Res.*, **68**, 37–62, <https://doi.org/10.1357/002224010793079004>.
- , J. C. McWilliams, and A. Shchepetkin, 2001: Open boundary conditions for long-term integration of regional oceanic models. *Ocean Modell.*, **3**, 1–20, [https://doi.org/10.1016/S1463-5003\(00\)00013-5](https://doi.org/10.1016/S1463-5003(00)00013-5).
- Marshall, J., A. Adcroft, C. Hill, L. Perelman, and C. Heisey, 1997: A finite-volume, incompressible Navier Stokes model for studies of the ocean on parallel computers. *J. Geophys. Res.*, **102**, 5753–5766, <https://doi.org/10.1029/96JC02775>.
- McWilliams, J. C., 2016: Submesoscale currents in the ocean. *Proc. Roy. Soc.*, **A472**, 20160117, <https://doi.org/10.1098/rspa.2016.0117>.
- , J. Gula, M. J. Molemaker, L. Renault, and A. F. Shchepetkin, 2015: Filament frontogenesis by boundary layer turbulence. *J. Phys. Oceanogr.*, **45**, 1988–2005, <https://doi.org/10.1175/JPO-D-14-0211.1>.
- Merrifield, M., and R. Guza, 1990: Detecting propagating signals with complex empirical orthogonal functions: A cautionary note. *J. Phys. Oceanogr.*, **20**, 1628–1633, [https://doi.org/10.1175/1520-0485\(1990\)020<1628:DPSWCE>2.0.CO;2](https://doi.org/10.1175/1520-0485(1990)020<1628:DPSWCE>2.0.CO;2).
- Nagai, T., N. Gruber, H. Frenzel, Z. Lachkar, J. C. McWilliams, and G.-K. Plattner, 2015: Dominant role of eddies and filaments in the offshore transport of carbon and nutrients in the California current system. *J. Geophys. Res. Oceans*, **120**, 5318–5341, <https://doi.org/10.1002/2015JC010889>.
- Nam, S., and U. Send, 2013: Resonant diurnal oscillations and mean alongshore flows driven by sea/land breeze forcing in the coastal Southern California Bight. *J. Phys. Oceanogr.*, **43**, 616–630, <https://doi.org/10.1175/JPO-D-11-0148.1>.
- Ohlmann, J. C., M. J. Molemaker, B. Baschek, B. Holt, G. Marmorino, and G. Smith, 2017: Drifter observations of submesoscale flow kinematics in the coastal ocean. *Geophys. Res. Lett.*, **44**, 330–337, <https://doi.org/10.1002/2016GL071537>.
- Orozco-Borbón, M. V., R. Rico-Mora, S. B. Weisberg, R. T. Noble, J. H. Dorsey, M. K. Leecaster, and C. D. McGee, 2006: Bacteriological water quality along the Tijuana-Ensenada, Baja California, México shoreline. *Mar. Pollut. Bull.*, **52**, 1190–1196, <https://doi.org/10.1016/j.marpolbul.2006.02.005>.
- O'Reilly, W., C. B. Olfe, J. Thomas, R. Seymour, and R. Guza, 2016: The California coastal wave monitoring and prediction system. *Coast. Eng.*, **116**, 118–132, <https://doi.org/10.1016/j.coastaleng.2016.06.005>.
- Pineda, J., 1994: Internal tidal bores in the nearshore: Warm-water fronts, seaward gravity currents and the onshore transport of neustonic larvae. *J. Mar. Res.*, **52**, 427–458, <https://doi.org/10.1357/0022240943077046>.
- Pringle, J. M., 2002: Enhancement of wind-driven upwelling and downwelling by alongshore bathymetric variability. *J. Phys. Oceanogr.*, **32**, 3101–3112, [https://doi.org/10.1175/1520-0485\(2002\)032<3101:EOWDUA>2.0.CO;2](https://doi.org/10.1175/1520-0485(2002)032<3101:EOWDUA>2.0.CO;2).
- Radermacher, M., M. A. de Schipper, C. Swinkels, J. H. MacMahan, and A. J. Reniers, 2017: Tidal flow separation at protruding beach nourishments. *J. Geophys. Res. Oceans*, **122**, 63–79, <https://doi.org/10.1002/2016JC011942>.
- Rasmussen, L. L., B. D. Cornuelle, L. A. Levin, J. L. Largier, and E. Di Lorenzo, 2009: Effects of small-scale features and local wind forcing on tracer dispersion and estimates of population connectivity in a regional scale circulation model. *J. Geophys. Res.*, **114**, C01012, <https://doi.org/10.1029/2008JC004777>.
- Rodriguez, A. R., S. N. Giddings, and N. Kumar, 2018: Impacts of nearshore wave-current interaction on transport and mixing of small-scale buoyant plumes. *Geophys. Res. Lett.*, **45**, 8379–8389, <https://doi.org/10.1029/2018GL078328>.
- Romero, L., Y. Uchiyama, J. C. Ohlmann, J. C. McWilliams, and D. A. Siegel, 2013: Simulations of nearshore particle-pair dispersion in Southern California. *J. Phys. Oceanogr.*, **43**, 1862–1879, <https://doi.org/10.1175/JPO-D-13-011.1>.
- , D. A. Siegel, J. C. McWilliams, Y. Uchiyama, and C. Jones, 2016: Characterizing storm water dispersion and dilution from small coastal streams. *J. Geophys. Res. Oceans*, **121**, 3926–3943, <https://doi.org/10.1002/2015JC011323>.

- Roughan, M., E. J. Terrill, J. L. Largier, and M. P. Otero, 2005: Observations of divergence and upwelling around point Loma, California. *J. Geophys. Res.*, **110**, C04011, <https://doi.org/10.1029/2004JC002662>.
- Shanks, A. L., S. G. Morgan, J. MacMahan, and A. J. H. M. Reniers, 2010: Surf zone physical and morphological regime as determinants of temporal and spatial variation in larval recruitment. *J. Exp. Mar. Biol. Ecol.*, **392**, 140–150, <https://doi.org/10.1016/j.jembe.2010.04.018>.
- Shchepetkin, A. F., and J. C. McWilliams, 2005: The Regional Oceanic Modeling System (ROMS): A split-explicit, free-surface, topography-following-coordinate oceanic model. *Ocean Modell.*, **9**, 347–404, <https://doi.org/10.1016/j.ocemod.2004.08.002>.
- Sinnett, G., and F. Feddersen, 2019: The nearshore heat budget: Effects of stratification and surfzone dynamics. *J. Geophys. Res. Oceans*, **124**, 8219–8240, <https://doi.org/10.1029/2019JC015494>.
- , —, A. J. Lucas, G. Pawlak, and E. Terrill, 2018: Observations of nonlinear internal wave run-up to the surf-zone. *J. Phys. Oceanogr.*, **48**, 531–554, <https://doi.org/10.1175/JPO-D-17-0210.1>.
- Steele, J. A., A. D. Blackwood, J. F. Griffith, R. T. Noble, and K. C. Schiff, 2018: Quantification of pathogens and markers of fecal contamination during storm events along popular surfing beaches in San Diego, California. *Water Res.*, **136**, 137–149, <https://doi.org/10.1016/j.watres.2018.01.056>.
- Suanda, S. H., and F. Feddersen, 2015: A self-similar scaling for cross-shelf exchange driven by transient rip currents. *Geophys. Res. Lett.*, **42**, 5427–5434, <https://doi.org/10.1002/2015GL063944>.
- , —, and N. Kumar, 2017: The effect of barotropic and baroclinic tides on coastal stratification and mixing. *J. Geophys. Res. Oceans*, **122**, 10–156, <https://doi.org/10.1002/2017JC013379>.
- , —, M. S. Spydell, and N. Kumar, 2018: The effect of barotropic and baroclinic tides on three-dimensional coastal dispersion. *Geophys. Res. Lett.*, **45**, 11–235, <https://doi.org/10.1029/2018GL079884>.
- Tilburg, C. E., and R. W. Garvine, 2003: Three-dimensional flow in a shallow coastal upwelling zone: Alongshore convergence and divergence on the New Jersey shelf. *J. Phys. Oceanogr.*, **33**, 2113–2125, [https://doi.org/10.1175/1520-0485\(2003\)033<2113:TFIASC>2.0.CO;2](https://doi.org/10.1175/1520-0485(2003)033<2113:TFIASC>2.0.CO;2).
- Uchiyama, Y., E. Y. Idica, J. C. McWilliams, and K. D. Stolzenbach, 2014: Wastewater effluent dispersal in Southern California bays. *Cont. Shelf Res.*, **76**, 36–52, <https://doi.org/10.1016/j.csr.2014.01.002>.
- Umlauf, L., and H. Burchard, 2003: A generic length-scale equation for geophysical turbulence models. *J. Mar. Res.*, **61**, 235–265, <https://doi.org/10.1357/002224003322005087>.
- Walter, R. K., and P. J. Phelan, 2016: Internal bore seasonality and tidal pumping of subthermocline waters at the head of the Monterey submarine canyon. *Cont. Shelf Res.*, **116**, 42–53, <https://doi.org/10.1016/j.csr.2016.01.015>.
- , C. B. Woodson, P. R. Leary, and S. G. Monismith, 2014: Connecting wind-driven upwelling and offshore stratification to nearshore internal bores and oxygen variability. *J. Geophys. Res. Oceans*, **119**, 3517–3534, <https://doi.org/10.1002/2014JC009998>.
- Warner, J. C., B. Armstrong, R. He, and J. B. Zambon, 2010: Development of a coupled ocean-atmosphere-wave-sediment transport (COAWST) modeling system. *Ocean Modell.*, **35**, 230–244, <https://doi.org/10.1016/j.ocemod.2010.07.010>.
- Warrick, J., and Coauthors, 2007: River plume patterns and dynamics within the Southern California bight. *Cont. Shelf Res.*, **27**, 2427–2448, <https://doi.org/10.1016/j.csr.2007.06.015>.
- Westerink, J. J., R. A. Luettich Jr., and N. Scheffner, 1993: Development of a tidal constituent database for the western North Atlantic and Gulf of Mexico. Rep. 3, ADCIRC: An advanced three-dimensional circulation model for shelves, coasts, and estuaries, Tech. Rep. DRP-92-6, Coastal Engineering Research Center, 150 pp., <https://apps.dtic.mil/sti/pdfs/ADA268685.pdf>.
- Wong, S. H. C., S. G. Monismith, and A. B. Boehm, 2013: Simple estimate of entrainment rate of pollutants from a coastal discharge into the surf zone. *Environ. Sci. Technol.*, **47**, 11 554–11 561, <https://doi.org/10.1021/es402492f>.
- Wu, X., G. Voulgaris, and N. Kumar, 2018: Shelf cross-shore flows under storm-driven conditions: Role of stratification, shoreline orientation, and bathymetry. *J. Phys. Oceanogr.*, **48**, 2533–2553, <https://doi.org/10.1175/JPO-D-17-0090.1>.
- Zaba, K., D. Rudnick, B. Cornuelle, G. Gopalakrishnan, and M. Mazloff, 2018: Annual and interannual variability in the California current system: Comparison of an ocean state estimate with a network of underwater gliders. *J. Phys. Oceanogr.*, **48**, 2965–2988, <https://doi.org/10.1175/JPO-D-18-0037.1>.